

THE LUMINOSITY FUNCTION OF YOUNG STAR
CLUSTERS IN “THE ANTENNAE” GALAXIES
(NGC 4038/4039)¹

BRADLEY C. WHITMORE, QING ZHANG², CLAUS LEITHERER, S. MICHAEL FALL,
Space Telescope Science Institute, 3700 San Martin Drive, Baltimore, MD 21218

Electronic mail: whitmore@stsci.edu

FRANÇOIS SCHWEIZER,

Carnegie Institution of Washington, Department of Terrestrial Magnetism, 5241 Broad Branch Road, NW,
Washington, DC 20015

Electronic mail: schweizer@dtm.ciw.edu

and BRYAN W. MILLER

Sterrewacht Leiden, Postbus 9513, 2300 RA Leiden, The Netherlands

Electronic mail: bmiller@strw.LeidenUniv.nl

Received:

¹ Based on observations with the NASA/ESA *Hubble Space Telescope*, obtained at the Space Telescope Science Institute, which is operated by the Association of Universities for Research in Astronomy, Inc., under NASA contract NAS5-26555.

² Also Johns Hopkins University, Charles and 34th St, Bloomberg Center, Baltimore, MD, 21218.

ABSTRACT

The Wide Field and Planetary Camera 2 of the *Hubble Space Telescope* has been used to obtain high-resolution images of NGC 4038/4039 that go roughly 3 magnitudes deeper in V than previous observations made during Cycle 2. These new images allow us to measure the luminosity functions (LF) of clusters and stars over a range of 8 magnitudes ($-14 < M_V < -6$). To first order the LF is a power law, with exponent $\alpha = -2.12 \pm 0.04$. However, using a variety of different techniques to decouple the cluster and stellar LFs, which overlap in the range $-9 \lesssim M_V \lesssim -6$, we find an apparent bend in the young cluster LF at approximately $M_V = -10.4$. Brightward of this magnitude the LF has a power law exponent $\alpha = -2.6 \pm 0.2$ while faintward the slope is $\alpha = -1.7 \pm 0.2$. The bend corresponds to a mass $\approx 1 \times 10^5 M_\odot$, only slightly lower than the characteristic mass of globular clusters in the Milky Way ($\approx 2 \times 10^5 M_\odot$). It is currently not feasible to determine the cluster LF fainter than $M_V \approx -8$, where individual stars are likely to dominate. The stellar LF in the range $-9 < M_V < -6$ is much steeper, with $\alpha = -2.9 \pm 0.1$, and is dominated by young red and blue supergiants. The star clusters of the Antennae appear slightly resolved, with median effective radii of 4 ± 1 pc, similar to or perhaps slightly larger than those of globular clusters in our Galaxy. However, the radial extents of some of the very young clusters (ages < 10 Myr) are much larger than those of old globular clusters (e.g., the outer radius of Knot S exceeds 450 pc). This may indicate that the tidal forces from the galaxies have not had time to remove some of the outer stars from the young clusters. A combination of the $UBVI$ colors, $H\alpha$ morphology, and GHRS spectra enables us to age-date the clusters in different regions of The Antennae. Star clusters around the edge of the dust overlap region appear to

be the youngest, with ages $\lesssim 5$ Myr, while clusters in the Western Loop appear to be 5 – 10 Myr old. Many star clusters in the northeastern star-formation region appear to be ~ 100 Myr old, with a LF in V that has shifted faintward by ~ 1.0 mag relative to the younger (0 – 20 Myr) clusters that dominate over most of the rest of the galaxy. A third cluster population consists of intermediate-age clusters (~ 500 Myr) that probably formed during the initial encounter responsible for ejecting the tails. A handful of old globular clusters from the progenitor galaxies are also identified. Most of these lie around NGC 4039, where the lower background facilitates their detection. Age estimates derived from GHRS spectroscopy yield 3 ± 1 Myr for Knot K (just south of the nucleus of NGC 4038) and 7 ± 1 Myr for Knot S in the Western Loop, in good agreement with ages derived from the $UBVI$ colors. Effective gas-outflow velocities from Knots S and K are estimated to be about $25 - 30 \text{ km s}^{-1}$, based on the above cluster ages and the sizes of the surrounding $H\alpha$ bubbles. However, the measured widths of the interstellar absorption lines suggest dispersion velocities of $\sim 400 \text{ km s}^{-1}$ along the lines of sight to Knots S and K.

Key Words: galaxies: star clusters, galaxies: interactions, galaxies: individual (NGC 4038/4039)

1. INTRODUCTION

One of the important early results from HST was the discovery of young, compact, extremely bright star clusters in merging galaxies (e.g., Holtzman et al. 1992, Whitmore et al. 1993). A large number of subsequent papers described similar objects in other mergers, starburst galaxies, and even barred galaxies (e.g., Holtzman et al. 1996, Stiavelli et al. 1998, Meurer et al. 1992, Conti & Vacca 1994, Barth et al. 1995; see Whitmore 1998 for a more complete summary). The nearest example of a full scale, ongoing merger is NGC 4038/4039, “The Antennae” galaxies. This represents perhaps our best chance for understanding what triggers bursts of star and cluster formation in mergers. In Whitmore & Schweizer (1995, hereafter Paper I), we found that the luminosity function (hereafter LF) $\phi(L)$ for point-like objects in NGC 4038/4039 was a power law, $\phi(L)dL \propto L^\alpha dL$, with an exponent of $\alpha = -1.78 \pm 0.05$ down to a limiting magnitude of about $M_V = -9.3$. This power-law shape agrees with the LF of Magellanic Cloud clusters and Galactic open clusters (Elson & Fall 1985) and the mass function of Giant Molecular Clouds (Harris & Pudritz 1994, Elmegreen & Efremov 1997), but differs from the LF of old globular clusters which is typically lognormal, i.e., a Gaussian distribution with a FWHM of ~ 3 mag in a number vs. magnitude plot. One of the possible explanations for this apparent difference is that we did not observe faint enough to see the turnover of the LF in NGC 4038/4039. Our new WFPC2 observations of this system go roughly 3 mag deeper in V than the earlier observations, allowing us to check whether the power-law shape of the LF continues to fainter magnitudes.

In Paper I we estimated that the mean effective radius (containing half the light) of

the young clusters in NGC 4038/4039 is 18 pc (for $H_0 = 50 \text{ km s}^{-1} \text{ Mpc}^{-1}$), although we also cautioned that “the measurement of cluster sizes is severely compromised by the poor image quality of the unrepaired telescope.” As van den Bergh (1995) pointed out, this mean effective radius is significantly larger than that of normal globular clusters in the Milky Way, which average around 3 pc. Indeed, Meurer et al. (1995) measured typical effective radii of 2 - 3 pc for young compact clusters in nearby starburst galaxies with cluster populations similar to NGC 4038/4039; these authors suggested that the larger distance and more severe crowding of clusters in NGC 4038/4039 had caused us to overestimate the radii. The repaired optics, availability of images from the better sampled Planetary Camera instead of the Wide Field Camera, and use of subpixel dithering all make the current data set vastly superior to the earlier WF/PC-1 observations for the purpose of measuring cluster sizes.

The current paper focuses on the LF, sizes, and ages of the clusters in NGC 4038/4039, as determined from broad-band images in *UBVI* and from UV spectroscopy of two knots using the Goddard High-Resolution Spectrograph (GHRS). Future papers will discuss the ages and the mass function of the clusters in more detail (Zhang & Fall, 1999), and will examine correlations with other physical quantities such as neutral hydrogen, the radio continuum, IR properties, X-ray emission, and the velocity field (Zhang et al. 1999).

In the following we adopt a Hubble Constant of $H_0 = 75 \text{ km s}^{-1} \text{ Mpc}^{-1}$, which places NGC 4038/4039 at a distance of 19.2 Mpc, corresponding to a distance modulus of 31.41 mag. Note that this distance differs from that in Paper I, where we adopted $H_0 = 50 \text{ km s}^{-1} \text{ Mpc}^{-1}$. At the distance of 19.2 Mpc the projected scale is $1'' = 93 \text{ pc}$, and 1 pixel on the

Planetary Camera covers 4.23 pc, while one pixel on the Wide Field Camera covers 9.26 pc.

2. OBSERVATIONS AND REDUCTIONS

2.1 WFPC2 Observations

As a followup to the Cycle 2, pre-refurbishment observations of NGC 4038/4039 with the WF/PC-1, an extensive set of much deeper observations were obtained with WFPC2 during Cycle 5 (proposal ID = 5962). On January 20, 1996, four separate exposures were taken through each of four broad-band filters, with total integration times of 4500 sec in F336W (referred to as the “U” filter), 4000 sec in F439W (“B”), 4400 sec in F555W (“V”), and 2000 sec in F814W (“I”). Photometric measurements obtained from these images were converted to Johnson U , B , V , and Cousins I passbands (note that this, too, is a change from Paper I where the F785LP measurement was converted to the Johnson I passband). The foreground reddening in the Milky Way toward NGC 4038/4039 is only 0.03 mag (Burstein & Heiles 1984) and has been ignored in this paper since it is negligible compared to the uncertainty in the value of the internal reddening. The internal reddening itself is highly variable throughout the galaxy. Two approaches are used below to minimize the effects of reddening due to dust (§4.1 and §4.2). The first approach is to divide the galaxies into regions with different levels of star formation and dust, and work primarily on the regions with minor levels of reddening and extinction. The second approach is to use reddening-free Q parameters to estimate and attempt to correct for extinction by dust.

The exposures in each filter were subpixel dithered to improve spatial resolution and to flatten the background, using pairs of exposures that were designed to be offset by $0.25''$

(i.e. 2.5 pixels on the Wide Field Camera [hereafter WFC] and 5.5 pixels on the Planetary Camera [hereafter PC]) from each other. The actual offsets on the PC measured using the STSDAS task *crosscor* varied from 5.21 pixels in Y to 6.26 pixels in X, in both cases on the F336W image. The mean offset for all the filters was 5.62 pixels. We note that the F336W observations had the longest separation in time (6 orbits), which may explain why they were the most discrepant from the target value of 5.5 pixels.

In addition to the long exposures, pairs of 60 sec subpixel dithered exposures were taken through the F439W, F555W, and F814W filters in order to recover the saturated peaks of the brightest regions in the long-exposure images. On January 13, 1996, narrow-band $H\alpha$ images were obtained through the F658N filter designed to pass the [N II] $\lambda 6584$ line at rest. At the redshift of NGC 4038/4039, this filter passes the $H\alpha$ line, as desired. We used the same strategy as for the broad-band images, but with a total exposure time of 3800 sec. In addition, two subpixel dithered images of Star-6 (see Paper I) of 30 sec duration each and centered on the PC were taken to provide a good point-spread-function (PSF). Additional images were taken with the Faint Object Camera (FOC), but are not used in the present paper.

Cosmic-ray tracks were removed using the STSDAS task *gcombine* on each matched pair of images, and then offset pairs were combined using the DRIZZLE software written by Fruchter & Hook (1998). A *pixfrac* parameter of 0.8 and scale parameter of 0.5 were used for the drizzling, thus converting each 800×800 image into a 1600×1600 image. Figure 1 shows an example of the separate and DRIZZLE-combined $H\alpha$ images around Knot G, along

with a deconvolved image computed via the routine *acoadd* and a TINY TIM PSF (Krist 1995). The advantage of subpixel dithering is readily apparent: the *acoadd* image clearly shows the most structure. However, since *acoadd* uses a non-linear algorithm that tends to amplify noise, we have not used this image for any measurements reported in the present paper.

After the subimages were drizzled together, bad pixels were removed using the hot-pixel lists obtained from the STScI WFPC2 web site and the task *warmpix*, and the saturated peaks of the brightest stars and clusters were replaced with properly scaled portions of the shorter-exposure images.

Photometric zeropoints were adopted from Table 28.1 of Version 3 of the *HST Data Handbook* (Voit 1997), and color transformations from Holtzman et al. (1995). Aperture corrections were non-trivial, since the clusters are clearly resolved and vary in size. An average cluster profile was determined from a number of isolated, high S/N clusters on each chip, and this profile was used to determine the aperture correction. While this should be roughly correct for a typical, relatively bright cluster, it should be recognized that the total magnitude for any particular cluster may be off by a couple tenths of a magnitude. An extreme case (Knot S) is discussed in §4.4.2. This magnitude uncertainty should have a very small effect on the LF presented in this paper, and has essentially no effect on the colors, since magnitudes within the same fixed apertures are used to form color indices. Aperture photometry was performed on all pointlike objects. The radii of the object aperture, the inner boundary of the background annulus, and the outer boundary were 4/10/15 pixels for

the PC and 3/7/11 pixels for the WFC. Note that these pixel triplets correspond to values on the original WFPC2 images that are half these numbers, since a scale of 0.5 was used in the DRIZZLE routine. Typical aperture corrections are 0.90 mag on the PC and 0.60 mag on the WFC. The fact that these corrections are larger than the corresponding aperture corrections for stars by 0.2 mag (WFC) to 0.4 mag (PC) shows that the clusters are fairly well resolved. A comparison with the measurements of V in Paper I for 13 bright clusters shows a mean difference of 0.19 mag, with the Paper I values being brighter. This reflects the difficulty of obtaining accurate photometry from spherically aberrated observations in a crowded field. The dispersion of the differences in V is about 0.12 mag. The comparison for $V-I$ color is better with a mean difference of only 0.01 mag and a dispersion of 0.06 mag.

The task *daofind* from the DAOPHOT package (Stetson 1987) was used to identify point-like objects (stars and clusters) from a median-divided DRIZZLE-combined V image (see Miller et al. 1997 for a discussion of the advantages of using a median-divided image). A comparison using aperture photometry from the two dithered images provided one last screening against the remaining cosmic rays, hot pixels, and chip defects. Completeness tests were performed for seven levels of the background on both the PC and WFC by using the task *addstar* in DAOPHOT to add artificial objects derived by using isolated, high S/N clusters from the same image. Figure 2 shows the resulting completeness fractions. The completeness thresholds used in this paper are defined as the magnitude where only half the artificial objects were identified. Corrections for non-optimal charge transfer efficiency on the CCDs of WFPC2 were made using the formulae by Whitmore & Heyer (1997).

The main advantages of the new observations with WFPC2 are the much improved spatial resolution and the correspondingly fainter thresholds for object detection, resulting in the identification of $\sim 14,000$ point-like sources as compared to ~ 700 in Paper I. The 20-fold increase in detected objects is partly due to the fact that individual stars become an important component faintward of $M_V \sim -9$, just beyond the absolute-magnitude threshold reached by our previous WF/PC-1 observations. Hence, in the outskirts of some of the richest clusters we are now able to study the clusters on a star-by-star basis, at least for the top few stellar magnitudes. Unfortunately, this also means that the problem of distinguishing between stars and clusters becomes a major issue, which will be discussed at length in the present paper.

Tables 1 through 4 gives the relative position, chip number, absolute magnitude M_V (assuming a distance modulus of 31.41), color indices, concentration index ΔV_{1-6} (i.e., the difference in V magnitudes measured in a 1 pixel and 6 pixel radius aperture, which provides a rough determination of the cluster size), and previous identification number (if it exists) from Paper I for the brightest 50 young cluster candidates, 25 intermediate-age clusters, 11 old globular clusters, and 13 foreground stars.

2.2 GHRIS Ultraviolet Spectroscopy

Ultraviolet spectra of Knots S and K were obtained with the GHRIS using Grating G140L on 1996 May 24. (See Rubin et al. 1970 for the original letter designations of the various knots.) Knot S was initially acquired with the Faint Object Spectrograph (FOS) using a 3-stage peak-up, followed by an automatic small-angle maneuver to move the center of

this giant cluster into the GHRS Large Science Aperture ($1''.7 \times 1''.7$). The centering accuracy is about $0''.35$, which corresponds to 1.5 GHRS science diodes. This in turn translates into a wavelength uncertainty of $\sim 1 \text{ \AA}$. The science exposure was centered at a wavelength of 1460 \AA and covered 286 \AA in wavelength. The exposure time was 45 min. Immediately following the exposure for Knot S, a blind offset was performed to Knot K, whose separation from S was measured on our WFPC2 images. A GHRS spectrum of K was taken with the same instrument configuration as for S, but with an exposure time of 50 min.

Knot S is dominated by a giant star cluster denoted as #405 in Paper I, and is listed as the second-brightest young cluster in NGC4038/4039 in Table 1. This cluster has a radius in excess of 450 pc (§4.4.2). The nearest major star cluster is #430, which is the 6th brightest young cluster in Table 1. It is 1.2 mag fainter in U and located $2''.3$ to the northeast of #405, whence it should not provide any measurable contamination within the $1''.7 \times 1''.7$ aperture. On the other hand, Knot K consists of two bright young clusters (#442 and #450, the 3rd and 4th brightest clusters in Table 1) that are separated by only $0''.7$, whence the recorded spectrum contains light from both clusters. The two clusters of Knot K have nearly identical colors and formed, therefore, probably at nearly the same time.

The two cluster spectra were analyzed with standard routines from the IRAF/STSDAS package. We found it unnecessary to recalibrate the *calhrs* pipeline products. After combining wavelength and flux data, we rebinned the wavelength scale to the restframe of NGC 4038/4039 ($v_{\text{hel}} = 1650 \text{ km s}^{-1}$; Paper I). Then the spectra were smoothed with a 5 pixel ($\sim 1.0 \text{ \AA}$) boxcar filter and normalized to unity by dividing them by a low-order

spline function that had been fit to line-free regions in the continuum. Wavelengths, equivalent widths, and line widths were measured in the normalized spectra using the *splot* package by fitting Gaussians to the observed profiles. The analysis of the spectra is presented in §4.5.

3. GENERAL APPEARANCE

Most of the major morphological features of The Antennae were discussed in Paper I, based on WF/PC-1 observations. Figure 3 shows a “true-color” image of The Antennae where the $U + B$ image is displayed in blue, the V image in green, and the I image in red. Figure 4 shows the same image as Figure 3 except that the $H\alpha$ image replaces the I image for the red display. Figure 5a shows a V image of The Antennae with the apparent locations of various regions of interest marked. The lettering follows the original definitions of most of these regions by Rubin et al. (1970) and in Paper I. Figure 5b identifies the brightest young cluster candidates, intermediate-age clusters, old globular clusters, and foreground stars. Enlargements of particularly interesting regions are included in Figure 6 ($UBVI$ image) and Figure 7 ($H\alpha$ image). Note the resemblance of the loops near the center of NGC 4039 (Figure 6, region A) to the loops seen around NGC 7252 (Schweizer 1982), on a scale roughly 20 times smaller than in NGC 7252. We may be seeing stars and gas being funneled into the center of the galaxy.

One of the most impressive features of Figure 3 is the fine structure of the dust filaments. While many of the filaments are found near regions of active star and cluster formation, there are also filaments in regions with little or no star formation. In particular, note the long, completely dark filament in the southeast quadrant of Figure 3. Conversely, there

are many regions of active star formation with little dust, based both on their appearance and the fact that many of these clusters have relatively unreddened colors. It appears that while regions of dense gas and dust are required to fuel star formation, once this begins the dust is fairly rapidly blown out or removed in some other way, leaving the regions relatively free of dust. We note that the most active regions of star formation appear to lie on the edges of the overlap region (e.g., regions B, C, D, E and F in Fig. 5). We also note that the northeastern star formation region appears to extend behind the overlap region, with its edge being visible along a line from region F to region B (see Figs. 3 and 5a). The northern part of NGC 4038 is relatively symmetric and does not appear to differ dramatically from a normal spiral galaxy, although it does feature a wider disk toward the northeast where the clusters appear to be more spread out. This suggests that this galaxy is at a relatively early stage of merging and violent relaxation has yet to occur.

Perhaps the most dramatic thing about the $H\alpha$ image of Figure 4 is the fact that one can immediately age-date the star formation in the various regions, since $H\alpha$ emission requires the presence of O and B stars to ionize the gas and these stars last less than ~ 10 Myr. The regions immediately adjacent to the overlap region appear to be the youngest, since the $H\alpha$ bubbles are quite small (see regions C and D in Fig. 7). The clusters in the Western Loop appear to be slightly older, since the $H\alpha$ bubbles are larger (see regions R+S+T in Fig. 7). Finally, the northeastern star formation region (around regions N and P) and the inner tail of NGC 4039 (region AA) are somewhat older still since they display little or no $H\alpha$ emission (best seen on Fig. 4). Another interesting result is that only large cluster complexes appear capable of blowing large $H\alpha$ bubbles, the largest of which measure

more than 1 kpc in diameter (see region G in Fig. 7). Isolated stars and small clusters have $H\alpha$ and continuum images that are roughly coincident.

Many of the cluster complexes, such as region T (Fig. 6), contain dozens of clusters. However, the second brightest cluster of The Antennae, Knot S (Fig. 6), appears to be an exception, since it is the dominant cluster of its region. Note the extensive halo of stars (typically with $-7 < M_V < -9$) surrounding this cluster out to nearly 500 pc, more than twice the tidal radius of the largest globular clusters in the Milky Way and M31 (§4.4). These extensive outer envelopes of stars are seen only around the brightest clusters and cluster complexes, presumably because these are also the youngest stellar aggregates (~ 10 Myr).

4. ANALYSIS

4.1 Separating Stars and Clusters

As briefly discussed in §1, Whitmore & Schweizer (1995) found that the LF of clusters in NGC 4038/4039 was a power law, $\phi(L)dL \propto L^\alpha dL$, with $\alpha = -1.78 \pm 0.05$ down to a limiting absolute magnitude of about $M_V = -9.3$. This is unlike the LF of old globular clusters which has a Gaussian profile with a peak around $M_V = -7.2$ and a width of ~ 1.4 mag. Several possible explanations for the apparent difference were discussed in Paper I, one being that we had not observed faint enough to see the expected turnover. The new WFPC2 observations of NGC 4038/4039 go roughly 3 magnitudes deeper than the earlier observations, allowing us to check whether the apparent power-law shape of the cluster LF continues to fainter magnitudes. Unfortunately, individual stars can have absolute

magnitudes as bright as $M_V \approx -9$, making the determination of the cluster LF at fainter magnitudes more difficult.

While it is possible in principle to separate most stars and clusters based on their apparent sizes, the crowded nature of the imaged field and the fact that the clusters are only slightly resolved results in some misidentifications. In practice, a more reliable method of identifying definite star clusters is to use a cutoff of $M_V < -9$ mag, which is brighter than all but a few of the brightest stars (Humphreys 1983). The top panels in Figure 8 show the concentration index ΔV_{1-6} , the $V-I$ vs. M_V color-magnitude diagram, and the $U-B$ vs. $V-I$ color-color diagram for the cluster-rich regions on the PC (i.e., regions T, S, R, and # 13; see Paper I for the latter identification). The evolutionary path of a Bruzual-Charlot (1996) cluster model with solar ($Z = Z_\odot$) metallicity and ages marked in logarithmic years is shown for reference. The choice of Z_\odot is mainly for illustrative purposes, although this value is typical of the few cluster metallicity estimates that have been made in similar systems (e.g., Schweizer & Seitzer 1998).

We find that the definite clusters (i.e., objects brighter than $M_V = -9$ mag) show a peak in their concentration-index histogram at $\Delta V_{1-6} \approx 3.0$, colors that fall in a fairly small range of $0.0 \lesssim V - I \lesssim 0.6$, and locations in the color-color diagram that define a tight clump with a mean age of about 10 Myr, based on the Bruzual-Charlot cluster models for Z_\odot . Only about 10 of the objects (or $\sim 5\%$) fall outside the tight clump and are probably individual stars (e.g., the mean value of $\overline{\Delta V}_{1-6} = 2.20 \pm 0.14$, with a scatter of 0.42 for these 10 objects, while $\overline{\Delta V}_{1-6} = 2.91 \pm 0.04$, with a scatter of 0.48 for the 163 objects falling near

the Bruzual-Charlot models). However, since the primary goal of the present paper is to determine the LF to as faint a magnitude as possible, we need to push beyond the $M_V = -9$ limit if possible.

The middle and bottom sets of panels in Figure 8 include all objects brighter than $M_V = -6$ for the cluster-rich and cluster-poor (i.e., west of R, S, and T) regions, respectively, on the PC. A comparison of the color-magnitude diagrams in the two regions shows that while the cluster-rich regions have a large number of objects brighter than $M_V = -9$, the cluster-poor regions have only two, and hence are likely to be dominated by individual young stars. In addition, most of the objects in the cluster-rich regions fall in a tight clump in the color-color plot, while the objects in the cluster-poor regions are more spread out and have relatively few members in the clump defined by the clusters in the top panel. Finally, and perhaps most importantly, the distributions of concentration indices are dramatically different (i.e., there are almost no objects with $\Delta V_{1-6} \approx 3.0$ in the cluster-poor regions, unlike the top panel where the peak at 3.0 indicates that the clusters are partially resolved), although there is considerable overlap in these histograms. Hence, in principle it should be possible to separate the stars from the clusters in a statistical sense by using the concentration-index and/or color information.

4.2 The Cluster LF

4.2.1 The Total LF of Point-Like Objects in NGC 4038/4039

Figure 9 shows the raw and completeness-corrected (but not reddening corrected,

see §4.2.2) LF for the objects on all four chips, as well as on the PC alone. The 50% completeness limits are indicated by arrows. The top panel shows the Number vs. m_V plot (in which a population of old globular clusters would have roughly a Gaussian distribution), the middle panel shows the $\log(\text{Number})$ vs. m_V plot (where a power law is a straight line), and the bottom panel shows the $\log(\text{Number})$ vs. m_V plot for the PC objects alone. The logarithmic LF for all the point-like objects on all four chips is reasonably linear, with a slope (power-law exponent) corresponding to $\alpha = -2.12 \pm 0.04$ when fit to the completeness limit at $M_V = -7.0$. This slope is steeper than the value found in Paper I ($\alpha = -1.78 \pm 0.05$), probably because there the spherical aberration made it difficult to detect the fainter objects and no completeness corrections were applied. We note that the values of α on all four chips are in relatively good agreement with each other ($\alpha = -2.17, -2.25, -2.03$, and -2.12 for Chips 1 through 4, respectively).

The relatively good linear fit over more than five magnitudes is somewhat surprising, since we believe that the object counts at fainter magnitudes are dominated by stars (see §4.1). However, the bright end of the LF from $M_V = -12.8$ to -10.4 is actually slightly steeper (i.e., $\alpha = -2.45 \pm 0.21$) than the overall LF, whereas the middle range from $M_V = -10.4$ to -7.4 is slightly flatter (i.e., $\alpha = -2.09 \pm 0.02$). While this slope difference is significant only at the 1.7σ level, we will present further evidence below for the reality of this apparent bend in the LF at $M_V \approx -10.4$.

The power-law fits employed in the present paper are based on least-squares fits weighted by the inverse of the variance in each bin. We also performed a variety of simul-

taneous two-slope power-law fits to quantify better the reality and position of the apparent bend in the LF. The total LF for all objects shown in Figure 9 is equally well fit by a single or a two-slope power law (i.e., the reduced χ^2 values are essentially identical).

4.2.2 Decoupling the LFs of Clusters and Stars

In an attempt to separate the cluster LF from the LF of the young stars in NGC 4038/4039, we have used four different methods. In essence, these methods consisted of:

(1) restricting the sample to the part of the LF brighter than $M_V = -9$, where clusters dominate (i.e., the approach used in §4.1),

(2) estimating the stellar LF from the cluster-poor regions, as shown in the bottom panel of Figure 8, and subtracting this from the total LF to determine the cluster LF,

(3) using the concentration (i.e., size) indices to attempt to isolate the clusters, and

(4) estimating the stellar LF based on the color information and subtracting it from the total LF to determine the cluster LF.

As we shall see, all four methods give reasonably similar results.

We begin by considering objects on the PC alone, since the better spatial sampling of the PSF there makes it easier to separate the stars from barely resolved clusters. The bottom panel of Figure 9 shows the LF for all objects on the PC. Restricting our attention

to the objects brighter than $M_V = -9$ yields a value of $\alpha = -2.17 \pm 0.06$. We again see a hint of an apparent bend at $M_V \approx -10.4$, with $\alpha = -2.95 \pm 0.29$ for the bright end of the LF and $\alpha = -2.07 \pm 0.04$ for the faint end.

Figure 10 shows the completeness-corrected LF for the cluster-rich regions on the PC, as well as the LF for the objects in cluster-poor regions. There are obvious differences between the two LFs, with a steep LF and only a single object brighter than $M_V = -9$ in the cluster-poor regions, and a much flatter distribution and 184 objects brighter than $M_V = -9$ in the cluster-rich regions. The power-law exponent is $\alpha = -2.01 \pm 0.11$ when the LF is fit with a single power law from $M_V = -11.4$ to -7.8 for the cluster-rich regions, and -2.92 ± 0.09 when the LF is fit from $M_V = -9.0$ to -6.0 for the cluster-poor regions. A two-slope power law provides a much better fit for the cluster-rich regions, with the parameters shown on the figure. The slopes brightward and faintward of the bend now differ by 4σ . The bend itself occurs at $M_V = -10.05 \pm 0.24$, brightward of where we expect contamination by stars or completeness corrections to become significant.

We can improve the statistics on a possible bend in the LF by using the same approach on all four chips, as shown in Figure 11. Figure 11b displays the LF for the cluster-rich regions only, while Figure 11a displays the total LF for all regions of NGC 4038/4039 for comparison. In Figure 11b, the dotted line shows the resulting cluster LF after the LF from the cluster-poor regions is used to estimate the stellar LF and subtract it from the total (normalizing the two by assuming that stars dominate at $M_V = -7.4$). The adopted normalization at $M_V = -7.4$ is not meant to imply that all objects at this absolute magnitude are stars, but

only to provide a lower bound to the possible cluster LF. The effect of the subtraction on the cluster LF is relatively small out to $M_V = -8.0$. The resulting slope of the cluster LF faintward of the bend is therefore bracketed between $\alpha = -1.76 \pm 0.03$ and $\alpha = -1.59 \pm 0.06$. The bend occurs at $M_V = -10.19 \pm 0.27$ in the former case and at $M_V = -10.40 \pm 0.25$ in the latter case. The change in slope at $M_V \approx -10.4$ represents a $\sim 4\sigma$ difference in both cases.

Figure 12 shows the same diagram as Figure 11, but with fits using a Schechter (1976) function to fit the observed LFs. This function provides similar or even slightly better fits to the data, with its knee roughly 1 mag brighter than the bend found using the two-slope power laws.

The third method for decoupling the stellar and cluster LFs uses size information. If we restrict the sample to objects on the PC with $\Delta V_{1-6} < 2.5$ (i.e., primarily stars), we find a steep stellar LF with corrected $\alpha = -2.42 \pm 0.06$ for a fit in the range from $-10.4 < M_V < -7.4$. If we restrict the sample to objects on the PC with $\Delta V_{1-6} > 2.5$ (i.e., primarily clusters), as shown in Figure 11c, we find a shallower cluster LF with $\alpha = -1.93 \pm 0.04$ in the same range. The two-power-law fit ($\chi^2 = 2.6$) provides a much better fit to the data than the single-power-law fit ($\chi^2 = 3.8$) does, with the bend occurring at $M_V = -10.25 \pm 0.38$.

The fourth method for decoupling the stellar and cluster LFs uses color information to isolate the stars. Figure 8 shows that when we isolate the definite clusters by including only the $M_V < -9$ objects, the resulting color-color diagram shows a tight clumping at a location in agreement with Bruzual-Charlot cluster models of ≈ 10 Myr age. The bottom

panel of Figure 8 shows that many individual stars have very different colors. We can use this fact to identify the objects that are almost certainly stars, and then subtract them from the total to estimate the number of clusters. This procedure only provides an upper limit to the number of clusters, since some fraction of the individual stars presumably have colors that lie in the cluster part of the color-color diagram.

The Antennae contain a large amount of dust, especially in the “Overlap Region” between the two galaxies (see Fig. 5a). Extinction from this dust affects the LF, while reddening affects age estimates. We can attempt to correct for the effects of dust by using reddening-free “Q” parameters (Becker 1938; Johnson & Morgan 1953) to estimate the intrinsic cluster colors, allowing us to estimate the extinction. The technique is described briefly below.

We employ the galactic reddening law by Mathis (1990). With the $UBVI$ colors, three independent reddening-free Q parameters can be defined (cf. Mihalas & Binney 1981) as

$$Q_1 = (U - B) - 0.72(B - V), \tag{1}$$

$$Q_2 = (B - V) - 0.80(V - I), \tag{2}$$

$$Q_3 = (U - B) - 0.58(V - I) \tag{3}$$

With these parameters, each object can be plotted on a Q - Q plot and compared with stellar population synthesis model tracks of cluster evolution (e.g., Bruzual & Charlot 1996) to determine its age and intrinsic colors. The difference between the observed and intrinsic

color, $E(B - V)$, is used to determine the extinction corrections for the various passbands.

Due to the nature of the cluster-model tracks and the observed scatter of data points, we have adopted the $Q_1 - Q_3$ plot as the primary tool in our attempt to decouple the stars from the clusters using color information. Figure 13a shows a two-color diagram for part of the northeastern star formation region and the corresponding $Q_1 - Q_3$ plot. Figure 13b shows the same plots for the cluster-rich regions on the PC. The $U - B$ vs. $B - V$ diagrams show that the regions are relatively dust free, since most of the objects fall near locations only slightly displaced from the Bruzual-Charlot model tracks (solid line). A typical value of $E(B - V)$ is 0.3, with typical values for $A_V = 1.0$. Small crosses with corresponding labels indicate the values of $\log(\text{age})$ along the Bruzual-Charlot models. A comparison of Figures 13a and Figure 13b indicates that there are a number of clusters with ages ≈ 100 Myr (i.e., $U - B \approx -0.3$, $B - V \approx 0.1$) in the northeastern star formation region, but essentially no clusters in this age range for the cluster-rich regions on the PC. More about this in §4.3 .

Besides the BC96 cluster-model tracks, loci for various types of stars are also included on the diagrams. As shown in the bottom panels of Figures 13a and 13b, stars tend to be located to the upper right of the evolutionary tracks for clusters, although there is some overlap between cluster models and stars (especially blue supergiants). Data points that are not located in the regions of stars or clusters (within the errors) are considered noise and are excluded from the sample.

Figure 14 shows similar plots for objects in the Overlap Region (see Fig. 5). As expected, the reddening due to dust moves the data points off the BC96 cluster-model track

in the $U-B$ vs. $B-V$ diagram. A typical value of $E(B-V)$ is 0.8. We find that most clusters in the Overlap Region have ages <20 Myr, with no significant population of clusters with ages ~ 100 Myr, similar to the results from Figure 13b. In addition, the offset from the model track in the $Q_1 - Q_3$ plot for the overlap region suggests a problem in either the galactic reddening law used to define the Q parameters, or the stellar evolution models. However, a comparison between the Leitherer & Heckman (1995) models and the BC96 models results in almost identical tracks up to approximately $\log t = 6.9$.

Figures 13 and 14 show that many individual stars should be identifiable by their colors, as was also apparent from Figure 8. Especially in the $Q_1 - Q_3$ plots, many types of stars lie well beyond the cluster-evolution tracks. Hence, we can estimate the number of stars by focussing on objects with values of $Q_3 > 0.0$ and $Q_1 > 0.0$. Using this technique, we find that at least 40% of the objects in NGC 4038/4039 are stars, which have subsequently been removed from Figures 13 and 14. This estimated percentage is a lower limit since some stars will have colors that make it impossible to distinguish them from clusters. Subtracting the resulting LF from the total LF we obtain an upper limit to the cluster LF. Figure 11d shows the result after the stars identified from the $Q_1 - Q_3$ plot have been subtracted. Once again a two-slope power law provides a better fit than a single power law, with a 5σ difference in the slopes.

Figure 11 shows that all four methods for decoupling the stellar and cluster LFs lead to cluster LFs with a bend at $M_V \approx -10.4$. Even the total LF, to which stars are likely to contribute significantly in the $M_V = -7$ to -8 range, shows a hint of this bend.

Based on these results, we conclude that the LF for young star clusters in NGC 4038/4039 is best represented by two power-law segments with indices of $\alpha = -2.6 \pm 0.2$ in the range $-12.9 < M_V < -10.4$ and $\alpha = -1.7 \pm 0.2$ in the range $-10.4 < M_V < -8.0$, respectively. It seems not possible at present to determine the cluster LF beyond $M_V = -8.0$, where stars are likely to dominate.

Figure 15 shows the dereddened and completeness-corrected LF for the cluster-rich regions on the PC. This compares fairly well with the top panel of Figure 10, supporting our claim that the extinction by dust is relatively small in most of the cluster-rich regions, and hence does not affect the LF very much. The bright end of the LF is still quite steep ($\alpha = -2.53 \pm 0.29$), the bend near $M_V \approx -10.4$ is more apparent, and the portion from $M_V = -10.4$ to -8.5 is flatter ($\alpha = -1.47 \pm 0.11$), presumably due to the removal of stars by the $Q-Q$ method discussed above. Unfortunately, with typical values of $A_V \approx 2 - 3$ mag for clusters in very dusty regions, it seems nearly impossible to obtain reliable cluster LFs in these regions.

Could the slight bend at $M_V \approx -10.4$ be the precursor to the observed peak at $M_V \approx -7.2$ in the LF of old globular clusters in elliptical galaxies (e.g., Whitmore 1997)? Based on our results in §4.3, a typical age for the young clusters in our sample appears to be about 10 Myr. The Bruzual & Charlot (1996) models would then predict that the clusters should fade by about 5 mag in V by the time they are 15 Gyr old (Whitmore et al. 1997, Fig. 18), rather than by the 3.2 mag difference between $M_V = -10.4$ and -7.2 . The agreement is better if we add an extinction correction of 1 magnitude to the bend (see

§4.2.2), resulting in a 4.2 mag difference.

A rough estimate of the mass corresponding to the bend in the LF can be made in a similar manner. Again adopting a typical age of 10 Myr, 1 mag of extinction, and using the solar metallicity BC96 models leads to a mass of $1 \times 10^5 M_{\odot}$ at the bend of the LF. This is somewhat lower than the characteristic mass of globular clusters in the Milky Way ($2 \times 10^5 M_{\odot}$; corresponding to the peak of the luminosity function for $M/L_V = 3$). Given various uncertainties in these simplistic calculations, such as the exact location of the bend, the age and metallicity to use for the calculation, uncertainties in the distance, and uncertainties in the Bruzual-Charlot models themselves, these estimates are probably compatible with the values expected of Milky Way globular clusters.

With the benefit of hindsight we note that the cluster LFs in NGC 7252 (Figs. 20b and 20d in Miller et al. 1997) and NGC 1275 (Carlson et al. 1998, Figs. 7 and 8) may also show a bend, but at about $M_V = -9.5$ to -10.0 . In addition, Zepf et al. (1999) find tentative evidence for a flattening in the cluster LF in the recent merger NGC 3256. Though taken alone none of these cases of lower-luminosity bends is compelling, in light of our new results for NGC 4038/4039 it appears that they may be part of a trend. We also note that the bend in the LF of the star clusters in NGC 4038/4039 is reminiscent of the bend seen in the LF of H II regions observed in several nearby galaxies (e.g., Kennicutt et al. 1989, Oey & Clarke 1998).

Meurer (1995) has suggested that the shape of the LF may evolve from an initial power law distribution to a log-normal distribution, due to the spread in the ages of the

clusters and the subsequent fading with time. This important topic will be addressed in a paper by Zhang & Fall (1999), who determine the cluster mass function by removing the effects of fading and extinction. They find that the luminosity function and mass functions are relatively similar in shape.

4.2.3 Effects of Emission Lines on UBVI Photometry

Emission lines can affect the broad-band colors measured for very young star clusters (e.g., Stiaivelli et al. 1998). For example, the F555W filter passband contains strong emission lines at $\lambda\lambda 4861, 4959, \text{ and } 5007 \text{ \AA}$, while the F814W filter passband does not contain any strong lines (i.e., its short wavelength cutoff lies at $\sim 7000 \text{ \AA}$, which excludes $\text{H}\alpha$). The F439W filter (i.e., B) passband is relatively less affected since it covers the range $4000 - 4700 \text{ \AA}$ and misses the strong emission lines at $\lambda\lambda 3727 \text{ and } 4861 \text{ \AA}$. Hence, it is mainly the V magnitudes of clusters in emission-line regions that are too bright, resulting in objects being measured too blue in $V-I$ and too red in $B-V$.

Figure 16 displays the $B-V$ vs. $V-I$ diagram for bright clusters on the PC, with objects with strong $\text{H}\alpha$ and weak (or absent) $\text{H}\alpha$ marked by different symbols. The various lines show the Bruzual-Charlot cluster-model tracks for three values of metallicity. While the objects with weak emission lines tend to fall along the Bruzual-Charlot tracks, those with strong emission lines are offset by about -0.2 in $V-I$. Hence, the presence of emission lines does affect the measured broad-band colors that include V , but the effect is relatively minor and its influence on the cluster LF should be nearly negligible. A comparison between LFs based on F439W, F555W, and F814W observations shows that this is indeed the case.

4.3 Cluster Ages

4.3.1 Evidence for Four Populations of Clusters in The Antennae

Simulations of merging galaxies suggest that star and cluster formation induced by the merger should be spread over several hundred million years, rather than happening in a rapid burst (e.g., Mihos et al. 1993). Hence, the resulting spread in cluster ages for ongoing mergers may provide an opportunity to study the early evolution of star clusters in a single system rather than having to intercompare several different galaxies.

There is evidence for four different populations of star clusters in The Antennae. The youngest population is most efficiently identified via the $H\alpha$ images. The presence of $H\alpha$ emission alone guarantees that the region contains clusters younger than ~ 10 Myr, since O and B stars must be present to ionize the gas. The size of the $H\alpha$ bubble can provide a further discriminant. In the cluster complexes bordering the Overlap Region of The Antennae (e.g., regions B, C, D, F; see Figure 5b), the $H\alpha$ and continuum images appear similar. Apparently there has not been enough time for the complexes to blow large bubbles, unlike in the slightly older regions of the Western Loop where there are large $H\alpha$ bubbles. Hence, we estimate that most of the clusters in the regions surrounding the Overlap Region are $\lesssim 5$ Myr old while the regions in the Western Loop (regions L, M, T, S, R, and G) have mean ages in the range 5 – 10 Myr.

The cluster ages derived from the $Q-Q$ analysis (§4.2.2) provide another age discriminant. These ages support the age estimates of ~ 10 Myr for the clusters in the Western Loop and those bordering the overlap regions. Roughly 70% of the bright clusters in our

sample have ages < 20 Myr. Unfortunately, because most of these clusters lie near a loop of the evolutionary tracks in the $Q_1 - Q_3$ diagram (i.e., clusters in the $\log[\text{age}]$ range of 6.5 – 7.2 have nearly the same colors), it is difficult to get a finer age discrimination. In addition, there is a tendency to overestimate the true fraction of young clusters, since they are more luminous and hence more easily detected than old clusters.

The second population of star clusters in The Antennae have ages of ~ 100 Myr based on the $Q-Q$ analysis. These objects are found primarily in the northeastern star formation region (Fig. 5). Figure 13a shows that roughly 2/3 of the bright clusters in this region have ages < 30 Myr and $\sim 1/3$ have ages of ~ 100 Myr. The distribution of ages appears to be continuous rather than bimodal. The $H\alpha$ image (Fig. 4) shows “streaks” of recent cluster and star formation in the northeastern star formation region which are embedded amongst objects showing no $H\alpha$ emission. The cluster candidates with ages ≈ 100 Myr can be seen in Figure 13a as a number of points centered around $U - B = -0.3$, $B - V = 0.1$. In the $Q_1 - Q_3$ diagram they correspond to the objects around $Q_1 = Q_3 = -0.5$. Figure 13b shows the corresponding diagrams for the cluster-rich regions on the PC, where the observations are consistent with having no clusters with ages ≈ 100 Myr.

Interestingly, the clusters of this second population appear to be more spread out than are the very tight clumps of young clusters (e.g., region T). Hence, it appears that the surface-number density of clusters is related to an age sequence, with younger regions having a higher cluster density than older regions.

The third population consists of star clusters with ages of ~ 500 Myr, based on the

Q – Q analysis. Unlike the first and second populations, these clusters appear to have formed in a separate burst, probably when the long tidal tails were ejected. Based on dynamical simulations (Mihos et al. 1995), the initial encounter occurred ~ 200 Myr ago, in general agreement with our estimate of ~ 500 Myr since the age estimates from both the dynamical and the Q – Q analysis are probably only good to about a factor of two.

We identify the older ~ 500 Myr population with the initial encounter, rather than the ~ 100 Myr population, since the tidal tails are likely to be the oldest relic of the encounter. The dynamical models suggest that following the initial encounter the two galaxies separated, and then later reengaged to form the current configuration. This picture is supported by the apparent lack of clusters with ages ~ 200 Myr, based on the Q – Q analysis.

The best examples of the third cluster population are found in the northwest corner of WF2, where three objects with $M_V \approx -10$ appear off the edge of the main galaxy (objects 5, 6, and 8 in Table 2; identified by squares in Fig. 5b). Figure 17 shows the color-magnitude and $Q_1 - Q_3$ plots for clusters in this region (which is called the Northwestern Extension in Fig. 5a). Note the clump of about 15 objects at $U - B = 0.2$ and $B - V = 0.25$, indicating mean ages of ~ 500 Myr. Most of the other clusters in this region appear to belong to the second population with ages ≈ 100 Myr. The three bright objects are amazingly similar in color ($B - V = 0.23, 0.26,$ and 0.21) and magnitude ($M_V = -9.86, -9.84,$ and -9.61), and all have ΔV_{1-6} values appropriate for clusters on the WF ($\Delta V_{1-6} = 2.02, 2.20,$ and 2.14). Assuming a present age of ~ 500 Myr, these clusters will be $M_V = -7.4$ after 14.5 Gyr, typical of old globular clusters. Note that these three clusters appear to be part of a

loop which connects back with the Western Loop around region T. Unfortunately, most of this loop lies to the northwest of the PC and is not covered by our WFPC2 images. The reconnection around region T appears to consist mainly of diffuse light from the original disk (referred to as the diffuse envelope of NGC 4038 in Paper I, see Malin 1992), although Figure 5b also shows a handful of intermediate-age clusters at the base of the loop (i.e., objects 4, 7, and 9 from Table 2 and Figure 5b; note the very tight range in magnitudes with objects 4 - 9 all being associated with this extended northwestern loop).

What are the ages of the clusters formed in the long tidal tails? Unfortunately, our images cover only a small portion of the southern tail in the southeastern corner of WF3. We find about a dozen objects, most of them showing $H\alpha$ emission that indicates ongoing star formation at the base of the tail. However, the only object bright enough to definitely be a cluster (number 12 in Table 2 with $M_V = -9.48$; see Fig. 5b) has an age of ~ 500 Myr, whence it was probably formed at the same time as the clusters in the northwestern extension, supporting our interpretation that this population was produced in the initial encounter that formed the tidal tails. There are about 30 other good candidates for intermediate-age clusters [i.e., $M_V < -9$ and $\log(\text{age}) = 8.4 - 9.0$] the brightest of which are listed in Table 2 and marked in Figure 5b.

The fourth population consists of old globular clusters from the original progenitor galaxies. Roughly 15 candidates were first identified based on their appearance in Figure 3 (i.e., slightly red with magnitudes in the range $M_V = -8$ to -11). Most of these were found around NGC 4039, where the background is lower. A check of their positions in the

Q – Q plot showed that 11 of these objects do indeed have ages of ~ 10 Gyr. These 11 objects are included in Figure 5b and Table 3. Taking into account the facts that (1) we are only seeing the bright end of the distribution (which generally peaks around $M_V = -7.2$), (2) we can only identify the objects in regions of low background (roughly 1/4 of the field), and (3) globular clusters tend to crowd around the centers of galaxies, we estimate that the total number of old globular clusters in The Antennae is at least an order of magnitude larger than our current sample of 11.

4.3.2 LFs vs. Age

In this section we compare the LFs for the various populations of clusters in The Antennae. Since the vast majority of the clusters belong to the youngest population (i.e., < 20 Myr), the LFs discussed earlier in the present paper are most representative of this population.

Figure 18 shows a comparison of the LFs for the cluster-rich regions on the PC (< 10 Myr old population) and for the fraction of the clusters with ages in the range 30 – 160 Myr, based on the Q – Q analysis. The latter clusters are found primarily in the northeastern star formation region, as discussed in the previous section. The two LFs are normalized at $M_V = -7.4$ to facilitate the comparison. We find a shift of about 1 mag at the bright end of the LF, which—scaled by the Bruzual-Charlot models and assuming a mean age of 10 Myr for the younger clusters—would be expected if the older population had a mean age of ~ 50 Myr, in reasonable agreement with our age estimate. In addition, the bend in the LF appears to occur at a slightly fainter absolute magnitude for the ~ 100 Myr population.

Because of the small number of objects, it is not possible to derive a meaningful LF for the population of old globular clusters. However, we note that the mean absolute magnitudes of the brightest few clusters from Table 2 are $M_V \approx -9$, typical of a population of old globular clusters.

4.4 Cluster Sizes

4.4.1 Effective Radii

As mentioned in §1, our earlier measurements of the effective radii of clusters in NGC 4038/4039 resulted in relatively large values ($\langle R_{\text{eff}} \rangle = 18$ pc, Paper I), which caused van den Bergh (1995) to question whether the clusters were young globular clusters or associations. In addition, Meurer et al. (1995) found that clusters in nearby starburst galaxies had typical effective radii of 2 – 3 pc, and cautioned that larger values measured for more distant galaxies may be due to crowding and insufficient resolution.

The current data are better suited for size measurements than our Cycle 2 observations for three reasons: (1) the repaired optics provide better PSFs, (2) the PC provides a better sampling of the PSF, and (3) subpixel dithering further improves the sampling.

Two different techniques have been used to estimate the effective radii R_{eff} of clusters. The first method models the observed profile with a King (1966) model, taking into account the spatial variations of the PSF across the chip and the different locations of objects relative to pixel centers (see Kundu & Whitmore 1998 for details). The images from the two dithering positions are measured separately since we have not yet calibrated this technique

for DRIZZLE-combined data. The estimates from the two images are then combined into a final value. This technique uses model PSFs from the TINY TIM program (Krist 1995) convolved with King models of various sizes. We note that the derived effective radii are roughly independent of the assumed concentration (Kundu & Whitmore, 1998). The use of high S/N PSFs from the actual PC image was not possible because of the lack of bright stars on the PC. However, one bright star (Star-6 from Paper I) was placed separately on the PC for a 30 s exposure to check the PSF at the center. There is good agreement with the PSF computed by TINY TIM.

Using this first technique we find that objects in star-dominated regions appear to have a mean $R_{\text{eff}} \approx 2$ pc. This finite radius probably results from a combination of three different effects. The first is that the PSF for the longer exposures in our observations may be slightly broader (perhaps due to jitter and breathing) than those used to model the PSF in TINY TIM, which are short exposures. The second is that in many regions crowding leads to overestimating the sizes of objects. And the third is that some of the faint objects have the right colors to be clusters rather than stars, whence they are likely to be slightly resolved. Because of these effects, we have chosen to make two size estimates designed to bracket the true cluster sizes. An upper limit is determined by taking the measured values of R_{eff} at their face value, with no correction for the fact that objects in star dominated regions appear to have sizes of ~ 2 pc. A lower limit is estimated by subtracting 2 pc from the measured R_{eff} to normalize objects in the star-dominated regions to have a mean value of 0 pc.

Figure 19 shows the resulting distributions of R_{eff} for objects in the star dominated regions (adjusted to 0 pc), for definite clusters in uncrowded regions of the PC (i.e., objects with $M_V < -9$), and for definite clusters throughout the PC. One important conclusion, based both on a visual inspection of objects with $R_{\text{eff}} > 10$ pc and a comparison of the histograms of Figure 19, is that essentially all objects with $R_{\text{eff}} > 10$ pc are affected by crowding (i.e., overlap with nearby companions), hence substantiating the concerns of Meurer et al. (1995). Virtually all cluster candidates in uncrowded regions have $R_{\text{eff}} = 0 - 10$ pc. Using $R_{\text{eff}} = 10$ pc as a cutoff results in a median value of $R_{\text{eff}} = 4 \pm 1$ pc for the clusters on the PC, where the quoted uncertainty represents the spread between the upper and lower limits discussed above. If the 10 pc cutoff is not applied the median value increases to 6 pc. Thus the median $R_{\text{eff}} = 4 \pm 1$ pc is only slightly larger than the median R_{eff} of globular clusters in the Milky Way (~ 3 pc, see van den Bergh 1996). Using the same technique for clusters on the WFC chips results in much larger scatter ($R_{\text{eff}} = 8 \pm 3$ pc) due to the more severe undersampling, whence our best estimates for R_{eff} are the PC measurements. Other recent estimates of cluster radii in mergers are $R_{\text{eff}} \approx 3 - 6$ pc (Schweizer et al. 1996; Miller et al. 1997; Whitmore et al. 1997; Carlson et al. 1998).

Our second technique for measuring R_{eff} makes use of the dithered data on all chips, but at the expense of adopting the simpler method of using Gaussian cluster profiles and the measured concentration indices ΔV_{1-6} to estimate the sizes, based on numerical experiments (same method as employed in Paper I). The advantages are the improved spatial resolution due to subpixel dithering and the fact that there are several bright stars on the WFC images to determine the PSF. In addition, the existence of old globular clusters on the same WFC

images makes a comparison between young and old clusters more straightforward. The mean values of ΔV_{1-6} measured for 10 of the 11 stars in Table 4 (dropping the object with $\Delta V_{1-6} = 2.17$) is $\langle \Delta V_{1-6} \rangle = 1.53 \pm 0.03$ mag (mean error). For the 11 candidate old globular clusters from Table 3 the mean value is $\langle \Delta V_{1-6} \rangle = 1.82 \pm 0.03$ mag. For 21 young clusters from Table 1 on the WFCs (dropping those with values >2.5 mag which are generally in crowded regions) it is $\langle \Delta V_{1-6} \rangle = 2.05 \pm 0.04$ mag. And for 20 intermediate-age clusters from Table 2 on the WFC (again, dropping those with a value >2.5 mag) it is $\langle \Delta V_{1-6} \rangle = 2.06 \pm 0.04$ mag. The corresponding values for the mean effective radii are $\langle R_{\text{eff}} \rangle = 3.0 \pm 0.3$ pc for old globular clusters, 4.6 ± 0.4 pc for young clusters, and 4.7 ± 0.4 pc for intermediate-age clusters. This shows that the clusters are relatively well resolved and supports our earlier claim that the young clusters appear to be slightly larger than old globular clusters, based on the PC measurements. We also note the good agreement between our measurements of R_{eff} for old globular clusters in NGC 4038/4039 and the values for globular clusters in the Milky Way quoted by van den Bergh (1996). The good agreement between estimates based on the simple method and the more sophisticated method using the King models is also reassuring. The relative independence of R_{eff} on the concentration index, as mentioned above, is probably responsible.

4.4.2 Outer Radii

While the effective radii of the young clusters appear to be only slightly larger than those of old globular clusters, the outer radii of a few of the young clusters in NGC 4038/4039 are much larger, presumably because they have not been whittled away by the tidal forces

of the galaxies yet. An extreme case is Knot S (#405 in Paper I), which measures over 900 pc in diameter. For comparison, only two globular clusters of the Milky Way have tidal radii larger than 200 pc (the record holder is NGC 5466 with $R_t = 240$ pc, see Djorgovski 1993), and all globular clusters in M31 measured so far have $R_t < 100$ pc (Cohen & Freeman 1991; Grillmair et al. 1996).

Figure 20 shows the surface-brightness profiles of Knot S (# 405), its neighbor Cluster #430, and the ~ 500 Myr old Cluster #225 for comparison. Knot S and Cluster #430 are highly luminous and lie in a relatively uncrowded region imaged by the PC. Their profiles were derived by a combination of aperture photometry near the center and multi-object photometry (Lauer 1988) further out. Both Knot S and #430 feature nearly pure power-law envelopes. Hence, we are only able to set upper and lower limits for the values of the core radius R_c and the tidal radius R_t , respectively, due to the limited spatial resolution near the center and the lack of a clear tidal cutoff in the outskirts. The values are $(R_c, R_t) = (<4.2$ pc, >450 pc) for Knot S and $(<4.6$ pc, >73 pc) for Cluster #430. Similarly, the values of the King (1966) concentration index $c \equiv \log(R_t/R_c)$ are $c > 2.03$ for Knot S and $c > 1.2$ for Cluster #430. The normal range for Milky Way globulars is $0.5 < c < 2.5$. Improved values of c will depend on measuring core radii from either deconvolved or new, higher-resolution images. We note in passing that Elson, Fall, and Freeman (1987) found that most of the young star clusters in the Large Magellanic Cloud, with ages in the range 8 – 300 Myr, also have profiles which are not tidally truncated.

In contrast, the intermediate-age Cluster #225 (object 4 from table 2) —which ap-

appears very isolated on a relatively featureless background—shows a distinct cutoff at $R_t \approx 50$ pc, a larger apparent core radius of $R_c = 5.6$ pc, and a central surface brightness lower in V by 5 mag than that of Knot S. During its lifetime of ~ 500 Myr, this cluster has apparently relaxed near the center, faded by several magnitudes, and lost its outermost stars due to tidal stripping. Yet, its concentration index $c \gtrsim 0.95$ places it well within the range of Milky Way globulars.

Finally, we note that whereas the detailed surface photometry confirms the integrated magnitude of #430 given in Table 1, the apparent magnitude of Knot S (object # 405) is $V = 15.63$, corresponding to $M_V = -15.8$, when integrated to the limit of $r = 450$ pc. Thus, Knot S is brighter than Table 1 would indicate (i.e., the aperture correction is much larger than the standard correction) and hence Knot S is a super cluster not only in size, but also in luminosity.

4.5 Ultraviolet Spectroscopy of Knots S and K

Figure 21 shows the spectra of Knots S and K in flux units, as described in §2.2. The spectral features are typical for young (< 10 Myr) star clusters. The strongest lines are broad stellar-wind features such as Si IV $\lambda 1400$ and C IV $\lambda 1550$, and narrow interstellar lines of lower ionization, like C II $\lambda 1335$ and Si II $\lambda 1526$. Note the double structure in most of the resonance lines. Strong Galactic halo absorption causes an additional component at a blueshift of about -1600 km s $^{-1}$ in the velocity frame of The Antennae. The only stellar *photospheric* features that are discernible above the noise are those of S V $\lambda 1502$, Si III $\lambda 1417$, and C III $\lambda 1427$.

4.5.1 UV Spectral Slope and Cluster Mass Estimates

Since Knot S and K harbor young star clusters with OB stars that dominate the UV light, the UV spectral slopes are not sensitive to stellar population properties, but instead are indicative of reddening by interstellar dust (Calzetti, Kinney, & Storchi-Bergmann 1994). Standard spectral synthesis models suggest $F_\lambda \propto \lambda^\beta$ with $\beta \approx -2.5$ between 1200 Å and 2000 Å for unreddened populations (Leitherer et al. 1999). We measure $\beta = -2.4 \pm 0.3$ and $\beta = -1.1 \pm 0.3$, for Knots S and K, respectively. Using these values, along with Calzetti’s (1997) extragalactic attenuation law, results in estimates of $E(B - V) = 0.01 \pm 0.04$ for Knot S and $E(B - V) = 0.12 \pm 0.04$ for Knot K. After dereddening, the intrinsic fluxes at 1500 Å of Knots S and K become 1.1×10^{-14} and 8.9×10^{-15} erg s⁻¹ cm⁻² Å⁻¹, respectively. Within the errors, both knots are equally bright at 1500 Å, and we adopt $F_{1500} = 1.0 \times 10^{-14}$ erg s⁻¹ cm⁻² Å⁻¹ which corresponds to a luminosity of $L_{1500} = 4.4 \times 10^{38}$ erg s⁻¹ Å⁻¹.

It is instructive to compare Knots S and K with other young clusters observed in the UV with IUE or HST. A few well studied cases are R136 in the LMC, NGC 4214#1, NGC 1569A, NGC 1705A, and NGC 1741B1, which have $L_{1500} = 6 \times 10^{37}$, 2×10^{38} , 3×10^{38} , 6×10^{38} , and 6×10^{39} erg s⁻¹ Å⁻¹, respectively (Leitherer 1998a). Hence, two of the brightest Antennae clusters have UV luminosities that are an order of magnitude more luminous than the central cluster of 30 Dor, but are rather unimpressive when compared with cluster B1 in NGC 1741.

4.6.2 Age Estimates from the Stellar-Wind Lines

We can use the standard stellar-wind line technique to determine the ages of the clusters in Knots S and K (e.g., Robert, Leitherer, & Heckman 1993; Leitherer et al. 1995). This technique utilizes the tight relation between the stellar far-UV radiation field and the wind density in massive hot stars. The winds are driven by momentum transfer from photospheric photons to wind material via absorption lines. Therefore the strength of lines such as Si IV $\lambda 1400$ and C IV $\lambda 1550$ correlates with the far-UV radiation field, and therefore with the relative proportion of hot, ionizing stars. The necessary synthesis models are taken from the Starburst99 package (Leitherer et al. 1999). Although a large suite of models was explored, we restrict our discussion to models in the parameter space favored by our previous discussion: (1) We assume that clusters contain single-burst stellar populations. (2) The mass spectrum is parameterized as a power law with a Salpeter slope between 1 and $100 M_{\odot}$. The lower mass cut-off is unimportant since we are only considering normalized quantities. (3) The metallicity of the evolution models is solar, and that of the library stars is about 0.2 dex subsolar, corresponding to the average interstellar metallicity within a few kpc from the Sun.

If these assumptions are made, the only free model parameter necessary to match the observed spectra is the age of the population. In Figure 22 we compare the spectra of Knots K and S with model spectra for cluster ages 1, 3, 5, 7, and 10 Myr. The most sensitive age indicator is the Si IV $\lambda 1400$ line, which is seen as a P Cygni profile from the winds of massive O supergiants in 3 – 5 Myr old populations. No P Cygni profile is observed at younger ages, and only a relatively weak blueshifted absorption appears after 5 Myr (see Leitherer et al. 1995). The observed Si IV $\lambda 1400$ profiles suggest that Knot K is 2 – 4 Myr old, and Knot S

is 6 – 8 Myr old. Note that the strong narrow absorption components (e.g., Si II λ 1526) are of interstellar origin. The behavior of the C IV λ 1550 line is consistent with our age estimate. The P Cygni profile of this line decreases monotonically with age, as opposed to that of the Si IV line. The C IV λ 1550 line is significantly stronger in Knot K than in S, supporting a younger age of the former.

These age estimates can be used in conjunction with the sizes of the evacuated H α bubbles (radius = $2''.2 \pm 0''.2$ around Knot S and $0''.85 \pm 0''.15$ around Knot K) to derive effective outflow velocities, v_{outflow} . The results are $v_{\text{outflow}} = 29 \pm 5 \text{ km s}^{-1}$ for Knot S and $v_{\text{outflow}} = 25 \pm 10 \text{ km s}^{-1}$ for Knot K.

The derived age of ~ 3 Myr for Knot K suggests that few supernova events will have occurred since the onset of the star-formation episode, whence we expect that the mechanical energy input into the interstellar medium is dominated by stellar winds. Is this enough to produce a global wind as suggested by the H α bubbles? A rough estimate of the energy budget with the Starburst99 package shows that a 3 Myr old population with 40% solar metallicity injects about 8×10^{52} erg into the gas, more than enough to form the observed bubble.

To summarize, based on their UV spectra we estimate that Knot S is 7 ± 1 Myr old, while Knot K is 3 ± 1 Myr old. These ages agree quite well with the age estimates based on the *UBVI* measurements and the *Q-Q* analysis described in §4.2.2, which yielded ages of ~ 5 Myr for both knots.

4.6.3 Kinematics of the Interstellar Medium

Figure 23 shows an enlarged portion of the spectra of Knots S and K, centered on the C II $\lambda 1335$ line. Two line components are visible in each knot: one intrinsic to The Antennae and the other intrinsic to the Galactic-halo component. The lines are offset from the nominal wavelength of 1334.53 \AA by about $+1 \text{ \AA}$, which agrees with the expected uncertainty in the wavelength zero point due to the target acquisition.

The mean measured line widths (FWHM) of the two components are 455 km s^{-1} for the Galactic halo lines and 630 km s^{-1} for the lines intrinsic to NGC4038/4039. The difference is significant and can be used to constrain the kinematics of the interstellar medium in NGC 4038/4039 along the lines of sight to the two knots. Other resonance lines (like Si II $\lambda 1526$) show similar behavior, but their widths and velocities are difficult to measure due to lower S/N ratios and blending. Taking the Galactic halo lines as indicators of the GHRS line-spread function (determined by the instrumental profile and the spatial structure of the stellar light), we can deconvolve the C II $\lambda 1335$ lines to estimate the true widths of the interstellar components in The Antennae. Superposition in quadrature, with the assumption that the Galactic halo line has an intrinsic FWHM = 100 km s^{-1} ; suggests a FWHM of 430 km s^{-1} for the interstellar components along the line of sight to Knots S and K.

This value for the velocity width is larger than that for halo lines in the Milky Way (i.e., maximum values $\approx 200 \text{ km s}^{-1}$). If the observed wavelength of the Galactic halo lines is used to correct the wavelength zero point, we find that the mean velocities of the interstellar C II $\lambda 1335$ along the line of sights to Knots S and K are 1706 km s^{-1} and 1678 km s^{-1} ,

respectively. These velocities are somewhat higher than the emission-line velocities from Rubin et al. (1970), which are $1619 \pm 5 \text{ km s}^{-1}$ and $1628 \pm 4 \text{ km s}^{-1}$, respectively.

5. SUMMARY

The WFPC2 on the Hubble Space Telescope has been used to obtain *UBVI* and $\text{H}\alpha$ images of the prototypical merging galaxies NGC 4038/4039 (“The Antennae”). UV spectra have also been obtained with the GHRS of two of the brightest star clusters. Over 14,000 point-like objects have been identified from the broad-band images. Based on their colors, a large fraction of these objects appear to be luminous young stars ($M_V > -8$) formed during the merger. The number of young star clusters is estimated to be between ~ 800 (using the conservative criterion that only objects brighter than $M_V = -9$ are definite clusters) and ~ 8000 (using an estimate based on subtracting all definite stars).

Our main results are as follows.

1. Using a variety of different techniques to decouple the cluster and stellar LFs (i.e., restricting the sample to $M_V < -9$, isolating cluster-rich regions, using size information, subtracting off stars identified via colors), we find that the cluster LF has two power-law segments and a bend at $M_V \approx -10.4$ (≈ -11.4 after making a correction for extinction). For absolute magnitudes brighter than $M_V \approx -10.4$ the power law is steep and has an exponent of $\alpha = -2.6 \pm 0.2$, while for the range $-10.4 < M_V < -8.0$ the power law is flatter with $\alpha = -1.7 \pm 0.2$. It seems not feasible at present to determine the cluster LF faintward of $M_V \approx -8$, where individual stars dominate. The stellar LF in the range

$-9 < M_V < -6$ appears dominated by young red and blue supergiants and is much steeper, with $\alpha = -2.9 \pm 0.1$.

2. Assuming a typical age of 10 Myr for the clusters, and 1 mag of extinction, the apparent bend in the LF corresponds to a mass $\approx 1 \times 10^5 M_\odot$, only slightly lower than the characteristic mass of globular clusters in the Milky Way ($\approx 2 \times 10^5 M_\odot$).

3. The clusters are slightly resolved, allowing us to determine their median effective radii, $R_{\text{eff}} = 4 \pm 1$ pc, similar to or slightly larger than those of globular clusters in our Galaxy. However, the outer radii of some of the clusters are much larger than usual. The diameter of Knot S is nearly 1 kpc, presumably because this cluster is very young (< 10 Myr) and hence has not yet lost many stars in the outer envelope by tidal forces.

4. The ages of young clusters can be estimated by a variety of methods, including *UBVI* colors, the presence of $H\alpha$, the size of $H\alpha$ bubbles, and GHRS spectra. The various methods give consistent results. The estimated ages indicate that the youngest clusters lie around the overlap region ($\lesssim 5$ Myr), clusters in the Western Loop are slightly older (5 – 10 Myr), and the northeastern star formation region contains clusters with ages ranging up to 100 Myr.

5. The LF for the ~ 100 Myr population is shifted faintward ~ 1.0 mag in V relative to that of the population of younger (0 – 10 Myr) clusters that dominate over most of the rest of the galaxy.

6. An intermediate-age population of star clusters (~ 500 Myr) has also been identi-

fied, with the most obvious members being found in the Northwest Extension. This Extension appears to be part of a loop that was probably extracted from the galaxy during the initial encounter responsible for forming the tail.

7. Eleven old globular clusters with $M_V < -8.0$ have been identified, primarily around NGC 4039, where there is less confusion with young clusters. By extrapolating to fainter magnitudes, and making a rough completeness correction, we estimate that the total number of old globular clusters in The Antennae is at least an order of magnitude larger.

8. Age estimates based on GHRS spectroscopy yield 3 ± 1 Myr for Knot K (near the center of NGC 4038) and 7 ± 1 Myr for Knot S in the Western Loop, in good agreement with the ages derived from the *UBVI* colors.

9. Effective gas-outflow velocities from Knots S and K are $v_{\text{outflow}} = 29 \pm 5$ km s⁻¹ and $v_{\text{outflow}} = 25 \pm 10$ km s⁻¹, respectively, based on the estimated cluster ages and the sizes of the surrounding H α bubbles. The widths of the interstellar lines indicate gas velocity dispersions of ~ 400 km s⁻¹ along the lines of sight, distinctly larger than those measured in absorption lines due to the Milky Way halo.

Thanks to Arunav Kundu for his help with the cluster size measurements. F.S. and B.W.M. thank Sandra Keiser and Michael Acierno for their cheerful and dedicated computer and programming support. F.S. also gratefully acknowledges partial support from the NSF through Grant AST 95-29263. A special thanks to the referee, Jon Holtzman, who's insightful

comments lead to several important improvements to the paper.

REFERENCES

- Barth, A. J., Ho, L. C., Filippenko, A. V., & Sargent, W.L.W. 1995, *AJ*, 110, 1009
- Becker, W. 1938, *Zeitschrift f. Ap.*, 15, 225
- Bruzual A. G., & Charlot, S. 1996, in preparation (BC96)
- Burstein, D., & Heiles, C. 1984, *ApJS*, 54, 33
- Calzetti, D. 1997, *AJ*, 113, 162
- Calzetti, D., Kinney, A.L. & Storchi-Bergmann, T., 1994, *ApJ*, 429, 582
- Carlson, M. N., Holtzman, J. A., and the WFPC2 IDT 1998, *AJ*, 115, 1778
- Cohen, J. G. & Freeman, K. C. 1991, *AJ*, 101, 483
- Conti, P. S., & Vacca, W. D. 1994, *ApJ*, 423, L97
- Djorgovski, S. 1993, in *Structure and Dynamics of Globular Clusters*, ed. S. G. Djorgovski & G. Meylan (San Francisco: ASP), p. 373
- Elmegreen, B. G. & Efremov, Y. N. 1997, *ApJ*, 480, 235
- Elson, R. A., & Fall, S. M. 1985, *ApJ*, 299, 211
- Elson, R. A. W., Fall, S. M. & Freeman, K. C. 1987, *ApJ* 323, 54
- Fruchter, A.S. and Hook, R.N., 1998, submitted to *PASP*, astro-ph/9808087.
- González-Delgado, R. M., Leitherer, C., Heckman, T. M., Ferguson, H. C., Lowenthal, J. D., & Robert, C. 1998, *ApJ*, 495, 692

Grillmair, C. J. et al. 1996, AJ, 111, 2293

Harris, W. E. & Pudritz, R. E. 1994, ApJ, 429, 177

Heckman, T. M., & Leitherer, C. 1997, AJ, 114, 69

Ho, L. C., & Filippenko, A. V. 1996, ApJ, 472, 600

Holtzman, J. et al. (the WFPC2 team) 1992, AJ, 103, 691

Holtzman, J. et al. (the WFPC2 team) 1995, PASP, 107, 1065

Holtzman, J. A. et al. (the WFPC2 team) 1996, AJ, 112, 416

Humphreys, R. M. 1983, ApJ, 269, 335

Johnson, H. L. & Morgan, W. W. 1953, ApJ, 117, 313

Kennicutt, R. C., Jr., Edgar, B. K., & Hodge, P. W. 1989, ApJ, 337, 761

King, I. R. 1966, AJ, 71, 64

Kinney, A. L., Bohlin, R. C., Calzetti, D., Panagia, N., & Wyse, R. F. G. 1993, ApJS, 86, 5

Krist, J. 1995, in *Astronomical Data Analysis, Software and Systems IV*, eds. R. Shaw et al.

(San Francisco: ASP), p. 349.

Kundu, A. & Whitmore, B. C. 1998, ApJ, 116, 2841

Lauer, T. R. 1988, ApJ, 325, 49

Leitherer, C. 1998a, in *Stellar Astrophysics for the Local Group*, ed. A. Aparicio, A. Herrero,

& F. Sánchez (Cambridge: CUP), 527

- . 1998b, in 38th Herstmonceux Conference, The Stellar Initial Mass Function, G. Gilmore & D. Howell (San Francisco: ASP), 61
- Leitherer, C. & Heckman, T. M. 1995, ApJS, 96, 9
- Leitherer, C., Robert, C., & Heckman, T. M. 1995, ApJS, 99, 173
- Leitherer, C., Schaerer, D., Goldader, J. D., González Delgado, R. M, Robert, C., Foo Kune, D., de Mello, D. F., Devost, D., & Heckman, T. M. 1999, ApJS, in press
- Malin, D. 1992, QJRAS, 33, 321
- Massey, P. 1998, in 38th Herstmonceux Conference, The Stellar Initial Mass Function, G. Gilmore & D. Howell (San Francisco: ASP), 17
- Mathis J. S. 1990, ARA&A, 28, 37
- Meurer, G. R. 1995, Nature, 375, 742
- Meurer, G.R., Freeman, K. C., Dopita, M. A. & Cacciari, C. 1992, AJ, 103, 60
- Meurer, G. R., Heckman, T. M., Leitherer, C., Kinney, A., Robert, C., Garnett, D. R. 1995, AJ, 110, 2665
- Mihalas, D. & Binney, J. 1981, Galactic Astronomy, (San Francisco: Freeman), p. 187
- Mihos, J. C., Bothun, G. D., & Richstone, D. O. 1993, ApJ, 418, 82
- Miller, B. W., Whitmore, B. C., Schweizer, F., & Fall, S. M. 1997, AJ, 114, 2381
- Oey M. S. & Clarke C. J. 1998, AJ, 115, 1543

- Pauldrach, A. W. A., Kudritzki, R.-P., Puls, J., & Butler, K. 1990, *A&A*, 228, 125
- Robert, C., Leitherer, C., & Heckman, T. M. 1993, *ApJ*, 418, 749
- Rubin, V. C., Ford, W. K. & D’Odorico, S. 1970, *ApJ*, 160, 801
- Schechter, P. 1976, *ApJ*, 203, 297
- Schweizer, F. 1982, *ApJ*, 252, 455
- Schweizer, F., Miller, B., Whitmore, B. C., & Fall, S. M. 1996, *AJ*, 112, 1839
- Schweizer, F. & Seitzer, P. 1998, *AJ*, 116, 2206
- Stetson, P. B. 1987, *PASP*, 99, 191
- Stiavelli, M., Panagia, N., Carollo, M., Romaniello, M. Heyer, I., Gonzaga, S. 1998, *ApJL*, 492, L135.
- Whitmore, B. C. 1997, in *The Extragalactic Distance Scale*, ed. M. Livio, M. Donahue, N. Panagia (STScI, Baltimore), 254.
- Whitmore, B. C., 1998, in *Galaxy Interactions at Low and High Redshift*, eds. J. E. Barnes & D. Sanders (ASP, San Francisco), in press
- Whitmore, B. C. & Heyer, I. 1997, WFPC2 ISR 97-08, (Space Telescope Science Institute, Baltimore)
- Whitmore, B. C., Miller, B. W., Schweizer, F., & Fall, S. M. 1997, *AJ*, 114, 1797
- Whitmore, B. C., & Schweizer, F. 1995, *AJ*, 109, 960 (paper I)

Whitmore, B. C., Schweizer, F., Leitherer, C., Borne, K., & Robert, C. 1993, AJ, 106, 1354

van den Bergh, S. 1995, Nature, 374, 215

van den Bergh, S. 1996, AJ, 112, 2634

Voit, M. 1997, HST Data Handbook (Space Telescope Science Institute, Baltimore)

Zepf, S. E., Ashman, K. M., English, J., Freeman, K. C., & Sharples, R. M. 1999, AJ, in
press

Zhang, Q., Fall, M., Whitmore, B. C., Leitherer, C., Schweizer, F., & Miller, B. W. 1999, in
preparation

Zhang, Q. & Fall, M., 1999, in preparation

FIGURE CAPTIONS

Figure 1 - Region around Knot G showing the two raw $H\alpha$ images along the bottom (shifted by 5.5 pixels in X and 5.4 pixels in Y), the image using the DRIZZLE software to combine the two images to the upper left, and the image using the ACOADD software to combine the two images to the upper right. See text for details.

Figure 2 - Completeness curves as determined from artificial star experiments for different background levels on the PC and WF. The background levels are given in units of DN (Data Number).

Figure 3 - “True color” image of NGC 4038/4039 using *UBVI* WFPC2 images (i.e., *U* + *B* for the blue display, *V* for the green display, and *I* for the red display; square root image).

Figure 4 - $H\alpha$ image (i.e., same as Fig. 3, but using the $H\alpha$ image in place of the *I* image for the red display).

Figure 5a - Identification image for the various regions discussed in the paper. See Rubin et al. (1970) or Paper I for original designations. Figure 5b - Identification image for the objects from Tables 1 – 4. Open circles mark young clusters (<30 Myr), open squares intermediate-age clusters (\sim 500 Myr), and filled circles old globular clusters. Plus signs mark foreground stars.

Figure 6 - “True color” enlargements of various regions of interest in NGC 4038/4039. Regions T and S have been rotated by 90 degrees with respect to Figure 3. Note that the figures have different scales (see the 2'' bar).

Figure 7 - $H\alpha$ image enlargements of various regions of interest in NGC 4038/4039.

Figure 8 - The top row of panels shows plots of the concentration index ΔV_{1-6} (a rough measure of cluster size), the $V-I$ vs. M_V color-magnitude diagram, and the $U-B$ vs. $V-I$ color-color diagram for objects with $M_V < -9$ (i.e., primarily clusters) in the cluster-rich regions on the PC (i.e., Knots T, S, R, and # 13). The arrow shows the reddening vector. The middle row of panels shows the same plots, but for objects with $M_V < -6$ (i.e., stars and clusters). The bottom row of panels is for objects with $M_V < -6$ in cluster-poor regions on the PC (i.e., primarily stars). Note how the ΔV_{1-6} and $U-B$ vs. $V-I$ plots can help separate stars and clusters.

Figure 9 - Raw LF (lower line) and completeness-corrected (but not reddening corrected) LFs for objects on all four chips, as well as on the PC alone (bottom panel). The 50% completeness limits are indicated by arrows. The top panel shows the Number vs. m_V plot (in which a population of old globular clusters would have a roughly Gaussian distribution), while the middle and bottom panels show $\log(\text{Number})$ vs. m_V plots (where a power law is a straight line).

Figure 10 - Completeness-corrected LF for the cluster-rich regions on the PC, as well as the LF for the objects in cluster-poor regions (primarily stars). The slopes and the location of the bend as determined by a two-slope power-law fitting function are included.

Figure 11 - Four attempts to separate the LFs of the clusters and stars. Panel A shows the total LF for NGC 4038/4039 (dominated by clusters at the bright end and by stars at the faint end). Panel B shows the LF for the cluster-rich regions throughout NGC 4038/4039, along with a version with an attempt to subtract off the stars (dotted line). Panel C shows the LF for objects on the PC that appear to be resolved (i.e., $\Delta V_{1-6} > 2.5$). Panel D shows

the cluster candidates based on the $Q-Q$ analysis. A change in the slope at $M_V \approx -10.4$ is seen in all four histograms. The two-slope power-law fits are shown.

Figure 12 - Same data as in Figure 11, but with Schechter-function fits.

Figure 13a - $U-B$ vs. $B-V$ plot and the corresponding $Q_1 - Q_3$ plot for a dust-poor region (northeastern star formation region). Evolutionary tracks for the BC96 model clusters are included, along with loci for various types of stars. The arrow shows the reddening vector. Small crosses with corresponding labels indicate the values of $\log(\text{age})$ along the Bruzual-Charlot models. As expected, the reddening from the dust moves the data points off the BC96 tracks. Figure 13b shows the same plots for the cluster-rich regions on the PC. Note the clusters with apparent ages ~ 100 Myr for the northeastern star formation region. This population is missing for the cluster-rich regions on the PC.

Figure 14 - Same as Figure 13, but for objects in the dust-rich Overlap Region. A comparison of the $Q_1 - Q_3$ plots in Figures 13 and 14 shows that the two regions both have clusters with ages ~ 10 Myr, but a sizable fraction of clusters with ages ~ 100 Myr is seen only in the northeastern star formation region.

Figure 15 - The dereddened and completeness-corrected LF for the cluster-rich regions on the PC. This compares fairly well with the top panel of Figure 10, supporting our claim that the extinction by dust is relatively small in most of the cluster-rich regions.

Figure 16 - $B-V$ vs. $V-I$ diagram for bright cluster candidates on the PC. Open circles mark clusters with strong $H\alpha$ emission, while filled circles mark clusters with weak or no $H\alpha$ emission. Note that the objects with weak $H\alpha$ emission fall nicely on the Bruzual-Charlot

model tracks, while objects with strong $H\alpha$ emission are offset by about -0.2 mag in $V-I$.

Figure 17 - $U-B$ vs. $B-V$ and $Q_1 - Q_3$ plots for the bright objects in the Northwestern Extension. Note the clump of about 15 objects with apparent mean ages of ~ 500 Myr (filled circles).

Figure 18 - A comparison of the dereddened LFs for objects in the cluster-rich regions on the PC (~ 10 Myr) and for the fraction of the clusters with ages in the range $30 - 160$ Myr, based on the $Q-Q$ analysis. The latter clusters are found primarily in the northeastern star formation region. The two LFs are normalized at $M_V = -7.4$ to facilitate the comparison. We find a shift in the LF of about 1 mag at the bright end.

Figure 19 - Distributions of effective radii R_{eff} for objects in star-dominated regions on the PC (normalized to 0.0 pc, see text), bright cluster candidates in uncrowded regions, and bright cluster candidates in crowded regions. This figure suggests that most of the objects with apparent $R_{\text{eff}} > 10$ pc are due to superpositions in crowded regions.

Figure 20 - Surface-brightness profiles for Knot S (i.e., Cluster #405), its neighbor Cluster #430, and the ~ 500 Myr old Cluster #225, all measured from the dithered PC image. No attempt at deconvolution has been made. Note the power-law nature of the profiles for Knot S and #430, the large extent of the envelope of Knot S (see parsec scale at top), and the distinct cutoff at $R_t \approx 50$ pc for Cluster # 225. The vertical scales for the three plots have not been altered; the central surface brightness of the older Cluster # 225 is lower in V by 5 magnitudes.

Figure 21 - GHRS spectra of Knots S and K obtained through the Large Science Aperture

($1''.7 \times 1''.7$). The wavelength scale is in the restframe of NGC 4038/4039.

Figure 22 -Comparison between the observed GHR spectra (thick lines) and model spectra based on evolutionary population synthesis (thin lines). The continuum level of each spectrum is at unity, with offsets of 0 to 7 added to each spectrum from the bottom to the top, respectively. The five models are for a single-star population with Salpeter IMF between 1 and $100 M_{\odot}$, with ages marked.

Figure 23 - Blowup from Figure 21 showing the C II $\lambda 1335$ lines in Knot S and K. The dashed vertical lines mark the nominal rest wavelength of C II at 1334.53 \AA and the wavelength of 1327.23 \AA , corresponding to a blueshift of -1642 km s^{-1} . The blue components represent absorption lines due to the Milky Way halo. Measured line widths (FWHM in km s^{-1}) are given for all lines.

Table1: Brightest Young Clusters (Age < 30 Myr)

no.	Δ R.A. ^a	Δ Dec ^a	chip	M_V ^b	$U - B$	$B - V$	$V - I$	ΔV_{1-6} ^c	Paper I # ^d
1	-22.77	23.15	2	-13.92	-0.61	0.02	0.49	1.75	605
2	-36.17	-3.29	1	-13.81	-0.61	0.06	0.33	3.66	405
3	0.00	0.00	2	-13.68	-0.72	0.06	0.06	1.95	442
4	0.38	0.60	2	-12.90	-0.67	0.05	0.07	1.96	450
5	39.86	-33.25	3	-12.71	-0.76	0.13	0.13	2.19	142
6	-34.61	-1.51	1	-12.55	-0.64	0.00	0.48	2.38	430
7	24.79	-2.30	3	-12.54	-0.79	-0.03	0.03	2.16	418
8	-26.26	-20.19	1	-12.40	-0.68	0.14	0.38	2.34	208
9	23.24	-53.92	3	-12.38	-0.73	0.39	0.34	3.02	89/90 ?
10	43.12	-1.60	3	-12.35	-0.61	0.14	0.69	1.79	428
11	23.73	-53.94	3	-12.34	-0.28	0.84	0.67	2.67	89/90 ?
12	-35.45	3.91	1	-12.32	-0.71	0.00	0.12	2.54	481
13	22.86	0.91	3	-12.21	-0.86	-0.06	-0.06	2.08	455
14	23.31	-54.02	3	-12.20	-0.79	0.37	0.28	3.10	89/90 ?
15	34.48	-8.75	3	-12.16	-0.57	0.28	0.73	1.84	342
16	42.39	-2.31	3	-12.14	-0.54	0.24	0.71	2.09	417
17	35.20	-39.61	3	-12.11	-0.73	0.06	0.04	2.77	120 ?
18	26.76	-4.62	3	-12.03	-0.67	0.25	0.31	2.28	389
19	35.26	-39.69	3	-11.98	-0.79	-0.06	0.03	2.91	120 ?
20	23.15	-53.59	3	-11.95	-0.65	0.53	0.46	3.34	89/90 ?
21	20.82	13.63	2	-11.82	-0.81	-0.06	-0.06	1.88	534
22	-35.42	-11.72	1	-11.78	-0.69	0.04	0.27	2.17	302
23	-13.70	-21.54	4	-11.78	-0.71	0.09	0.19	2.18	200
24	18.42	13.87	2	-11.77	-0.56	0.09	0.59	1.76	537
25	-14.23	-18.00	4	-11.75	-0.70	0.26	0.42	2.25	236
26	21.75	-54.27	3	-11.75	-0.55	0.31	0.73	2.05	88
27	1.92	-14.91	3	-11.72	-0.58	0.09	0.56	2.12	265
28	-10.47	-10.69	2	-11.70	-0.72	0.09	0.18	2.38	313
29	-36.10	-3.01	1	-11.69	-0.79	0.09	0.56	4.08	405 ?
30	22.87	-54.46	3	-11.67	-0.69	0.14	0.14	2.94	86/87 ?
31	-36.89	-10.75	1	-11.66	-0.69	0.04	0.45	2.76	317
32	-4.24	32.20	2	-11.66	-0.77	0.03	0.12	2.07	690
33	22.91	-54.21	3	-11.63	-0.67	0.17	0.09	3.32	86/87 ?
34	1.33	7.05	2	-11.61	-0.24	0.64	0.84	2.57	503 ?
35	37.37	-13.40	3	-11.60	-0.55	0.20	0.59	2.21	282
36	2.22	-58.50	4	-11.58	-0.25	0.56	1.15	2.24	61
37	39.18	-9.07	3	-11.57	-0.61	0.11	0.45	1.72	336
38	1.37	6.82	2	-11.50	-0.07	0.82	1.00	2.95	503 ?
39	22.86	-54.52	3	-11.48	-0.68	0.15	0.24	3.10	86/87 ?

Table1: continued

no. # ^c	Δ R.A. ^a	Δ Dec ^a	chip	M_V ^b	$U - B$	$B - V$	$V - I$	ΔV_{1-6} ^c	Paper I # ^d
40	-37.36	-9.04	1	-11.46	-0.70	0.06	0.17	2.61	338/339/340 ?
41	21.56	0.06	3	-11.42	-0.67	0.05	0.38	1.89	443
42	3.31	14.22	2	-11.41	-0.64	0.09	0.48	2.62	538
43	-24.56	26.51	2	-11.40	-0.65	0.03	0.61	2.16	640
44	-23.15	19.54	2	-11.38	-0.31	0.58	1.15	1.92	561
45	6.51	-58.40	4	-11.38	-0.63	0.22	0.20	2.39	62
46	-37.62	-9.23	1	-11.37	-0.79	-0.19	-0.15	2.65	338/339/340 ?
47	-35.67	3.74	1	-11.37	-0.68	0.05	0.12	2.42	481
48	41.61	-12.97	3	-11.37	-0.47	0.23	0.65	2.03	285
49	-22.94	-15.73	1	-11.34	-0.56	0.28	0.32	2.39	253
50	-35.31	3.96	1	-11.33	-0.80	-0.05	0.22	3.13	485

^a Following the convention used in Paper I, the coordinates are the offsets in " from Object # 442, which is near the nucleus of NGC 4038. The equatorial coordinates of Object # 442 are R.A. = $12^h 01^m 52.97^s$ and DEC = $-18^\circ 52' 08.29''$ (J2000 coordinates in the coordinate frame of the Guide Star Catalog).

^b Absolute magnitude in the V band using a distance modulus of $m-M = 31.41$. The values are not corrected for extinction.

^c ΔV_{1-6} on the PC (i.e., chip 1) cannot be directly compared with ΔV_{1-6} on the WFC (i.e., chips 2,3,4) since the pixel scale and PSF are different.

^d Question marks indicate cases where a one-to-one matching was problematic, generally because of differences in spatial resolution between the Cycle 2 and Cycle 5 observations.

This figure "whitmore_1.jpg" is available in "jpg" format from:

<http://arxiv.org/ps/astro-ph/9907430v2>

Table 2: Intermediate-age Cluster Candidates ($0.25 < \text{Age} < 1 \text{ Gyr}$)

no.	$\Delta \text{ R.A.}$	$\Delta \text{ Dec}$	chip	M_V^a	$U - B$	$B - V$	$V - I$	ΔV_{1-6}^b	Paper I # ^c
1	43.15	1.62	3	-10.61	0.12	0.29	0.51	2.13	462
2	5.21	31.60	2	-10.18	0.07	0.18	0.41	1.97	688
3	5.12	27.84	2	-9.95	0.12	0.19	0.4	2.11	656
4	-35.84	-18.75	1	-9.90	0.10	0.15	0.36	2.52	225
5	-28.62	40.47	2	-9.86	0.17	0.23	0.45	2.02	—
6	-27.50	39.15	2	-9.84	0.16	0.26	0.47	2.20	—
7	-20.92	-22.17	4	-9.83	0.10	0.27	0.51	2.06	196
8	-32.85	44.60	2	-9.61	0.13	0.21	0.48	2.14	—
9	-24.56	-20.78	1	-9.56	-0.03	0.19	0.38	2.68	204
10	21.56	22.45	2	-9.56	0.03	0.23	0.39	2.09	600
11	1.30	34.84	2	-9.49	0.24	0.28	0.48	2.11	703
12	77.68	-27.02	3	-9.48	0.16	0.26	0.40	2.60	163
13	9.03	-5.96	3	-9.41	0.99	1.42	2.04	1.53	376
14	48.00	1.41	3	-9.32	0.00	0.30	0.46	2.29	457
15	35.85	14.58	2	-9.20	-0.04	0.16	0.47	2.16	540
16	-31.92	-7.32	1	-9.20	0.14	0.26	0.47	2.70	358
17	-28.47	25.10	2	-9.16	0.15	0.27	0.49	2.09	625
18	-5.74	44.05	2	-9.14	0.01	0.25	0.45	2.10	728
19	38.06	0.17	3	-9.12	0.04	0.28	0.57	2.11	446
20	30.95	17.52	2	-9.06	0.04	0.17	0.41	1.97	555
21	-37.63	-3.62	1	-9.05	-0.08	0.07	0.12	2.00	?
22	34.61	16.74	2	-8.95	-0.03	0.19	0.37	2.15	552
23	-1.19	20.01	2	-8.89	0.17	0.34	0.57	2.00	565
24	-7.36	-70.51	4	-8.87	0.52	0.85	1.08	1.72	23
25	-0.11	42.35	2	-8.86	-0.04	0.15	0.44	2.22	727

^a Absolute magnitude in the V band using a distance modulus of $m-M = 31.41$. The values are not corrected for extinction.

^b ΔV_{1-6} on the PC (i.e., chip 1) cannot be directly compared with ΔV_{1-6} on the WFC (i.e., chips 2,3,4) since the pixel scale and PSF are different.

^c The question mark for object 21 indicates that no counterpart was found on the Paper I list, presumably because this object was close to # 405 which is the second brightest object from Table 1. Dashes indicate cases where the objects were off the edge of the Cycle 2 observations.

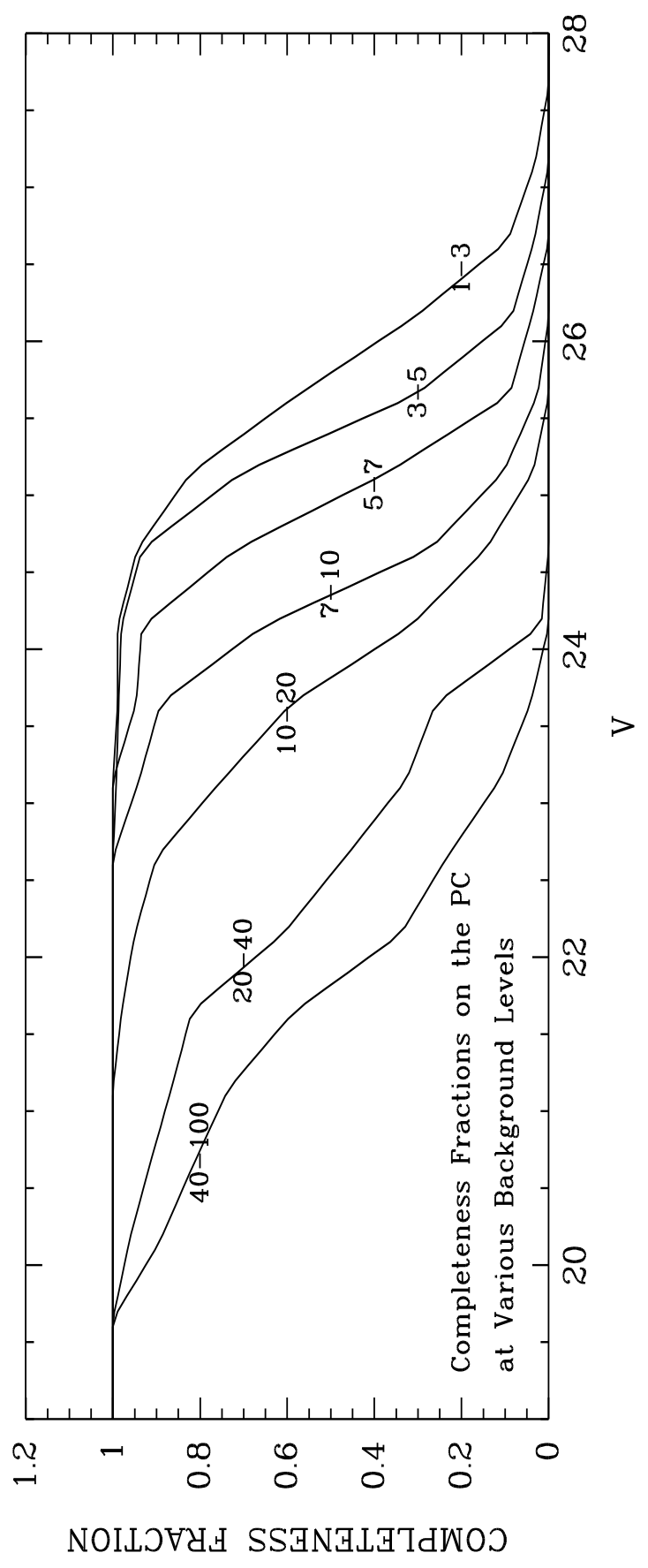
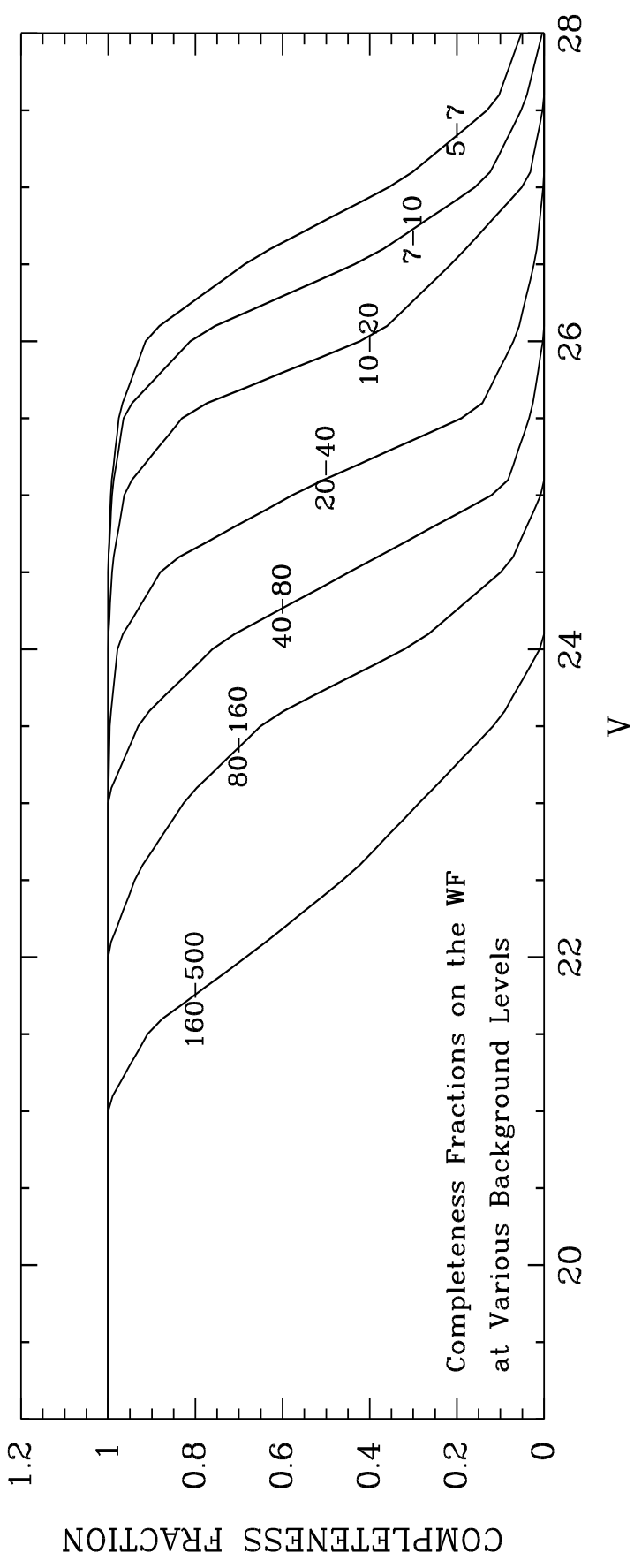


Table 3: Old Globular Clusters

no.	Δ R.A.	Δ Dec	chip	M_V	$U - B$	$B - V$	$V - I$	ΔV_{1-6}	Paper I
1	14.49	-35.70	3	-10.25	0.19	0.71	0.91	1.66	133
2	-16.63	6.71	2	-9.00	0.02	0.67	0.89	1.86	502
3	-16.52	-91.44	4	-8.87	-0.05	0.79	1.03	1.89	4
4	1.02	54.90	2	-8.86	-0.02	0.69	0.87	1.84	—
5	60.67	-38.38	3	-8.86	0.13	0.80	1.00	1.86	123
6	-21.29	-96.85	4	-8.72	0.27	0.79	1.02	1.83	—
7	-30.63	-72.89	4	-8.64	0.15	0.94	1.23	1.94	22
8	-21.79	-96.98	4	-8.60	0.46	0.92	1.21	1.59	—
9	-28.00	-73.98	4	-8.09	0.17	0.95	1.13	1.82	—
10	2.54	-88.82	4	-7.84	0.11	0.94	1.22	1.83	—
11	-47.56	-68.09	4	-7.72	0.09	0.79	0.95	1.92	—

This figure "whitmore_3.jpg" is available in "jpg" format from:

<http://arxiv.org/ps/astro-ph/9907430v2>

Table 4: Foreground Stars

no.	Δ R.A.	Δ Dec	chip	m_V	$U - B$	$B - V$	$V - I$	ΔV_{1-6}	Paper I
1	-18.26	34.73	2	16.62	0.74	0.97	1.09	1.45	star 6
2	-44.37	49.01	2	19.22	-0.04	0.60	0.71	1.69	—
3	26.91	22.30	2	19.77	0.72	1.11	1.31	1.44	598
4	46.10	-35.37	3	20.66	1.42	1.37	2.71	1.57	134
5	10.84	-16.32	3	20.79	-0.02	0.61	0.76	1.46	248
6	81.31	-44.30	3	21.72	1.07	1.20	1.46	1.63	110
7	-35.70	-45.45	4	21.99	1.71	1.29	1.96	1.43	star 4
8	-11.91	-39.73	4	22.50	0.58	0.63	0.81	2.17	121
9	-55.45	-55.81	4	22.82	1.07	1.58	3.17	1.48	star 3
10	-54.51	-73.36	4	22.93	0.47	1.50	2.18	1.49	—
11	-7.59	49.57	2	23.02	0.87	1.37	2.25	1.68	—
12	-59.15	-68.56	4	23.10	0.17	0.75	0.96	1.50	—
13	0.77	-49.36	4	23.65	1.13	1.53	1.51	1.56	—

This figure "whitmore_4.jpg" is available in "jpg" format from:

<http://arxiv.org/ps/astro-ph/9907430v2>

This figure "whitmore_5a.jpg" is available in "jpg" format from:

<http://arxiv.org/ps/astro-ph/9907430v2>

This figure "whitmore_5b.jpg" is available in "jpg" format from:

<http://arxiv.org/ps/astro-ph/9907430v2>

This figure "whitmore_6a.jpg" is available in "jpg" format from:

<http://arxiv.org/ps/astro-ph/9907430v2>

This figure "whitmore_6b.jpg" is available in "jpg" format from:

<http://arxiv.org/ps/astro-ph/9907430v2>

This figure "whitmore_7a.jpg" is available in "jpg" format from:

<http://arxiv.org/ps/astro-ph/9907430v2>

This figure "whitmore_7b.jpg" is available in "jpg" format from:

<http://arxiv.org/ps/astro-ph/9907430v2>

